# Performance Evaluation of CdZnTe Based Improved X-ray Detector on SharjahSat-1 Cubesat

Ali Mürteza Altıngün

Physics Seminars
IPHC

2 July, 2023

# SharjahSat-1 Cubesat

- SharjahSat-1, a 3U cubesat with scientific mission in collaboration among SAASST, US, ITU, and SU.
- Scientific payload, a Cadmium-Zinc-Telluride (CdZnTe, or CZT) based improved X-Ray Detector (iXRD)
  - monitoring bright X-ray sources, such as X-Ray binary systems, the Solar hard X-ray flares
- optical cameras for low-resolution remote sensing applications as secondary payload
- Launched in January in 2023 to SSO with approx. 500 km altitude

# The iXRD

- The iXRD → improved version of XRD (X-Ray Detector) employed as a scientific payload for the 2U BeEagleSAT cubesat [1]
  - $2.54 \times 2.54 \times 0.5$ cm$^3$ pixellated CdZnTe crystal ($16 \times 16$ pixels - a planar cathode)
  - Energy range of 20 keV - 200 keV
  - A square hole Tungsten collimator providing 4.26° field of view
  - An aluminum plate of 0.3 mm as an optical blocker
  - A 2 mm thick tungsten plate as a shielding against radiation

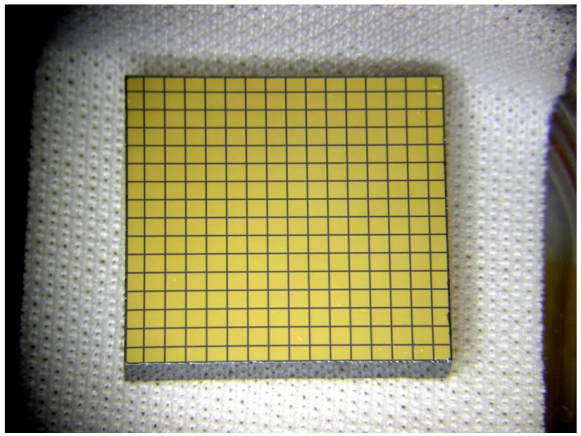

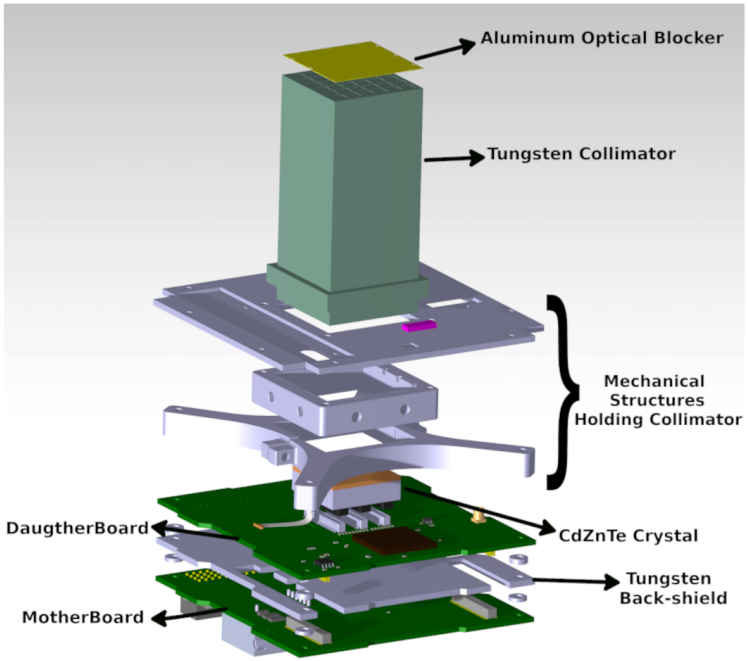

# The iXRD Readout

- A single RENA 3b ASIC (application specific integrated circuit) as readout
  - 36 channels, low noise, selectable-polarity, signal ranges and peaking time on a channel by channel basis.
  - controlled by MSP 430 microcontroller
- MotherBoard (MB): MSP, SD cards for data storage, communication circuitry, and HV supply.
- DaughterBoard (DB): crystal, RENA ASIC, voltage regulators, and a thermocouple.

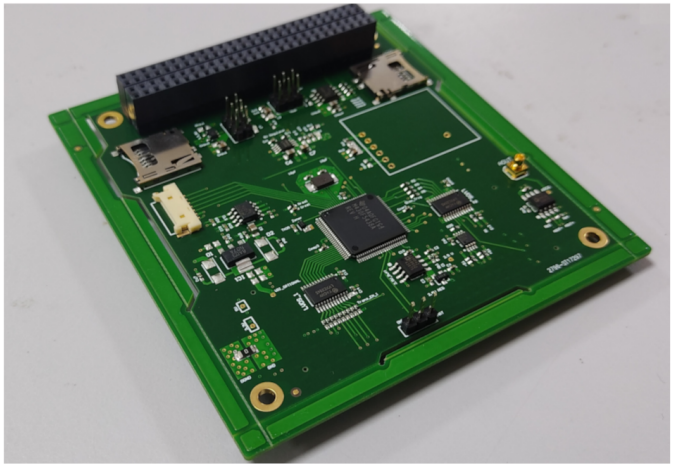

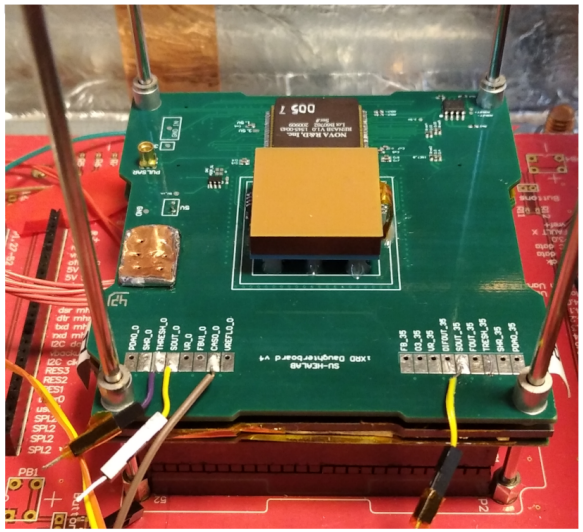

# The iXRD Readout

- Having 36 channels in RENA, 35 larger pixels created, one channel assigned to cathode signal
  - single (one pixel), small (6 pixels), medium (8-9 pixels), and large (10-12 pixels) channels

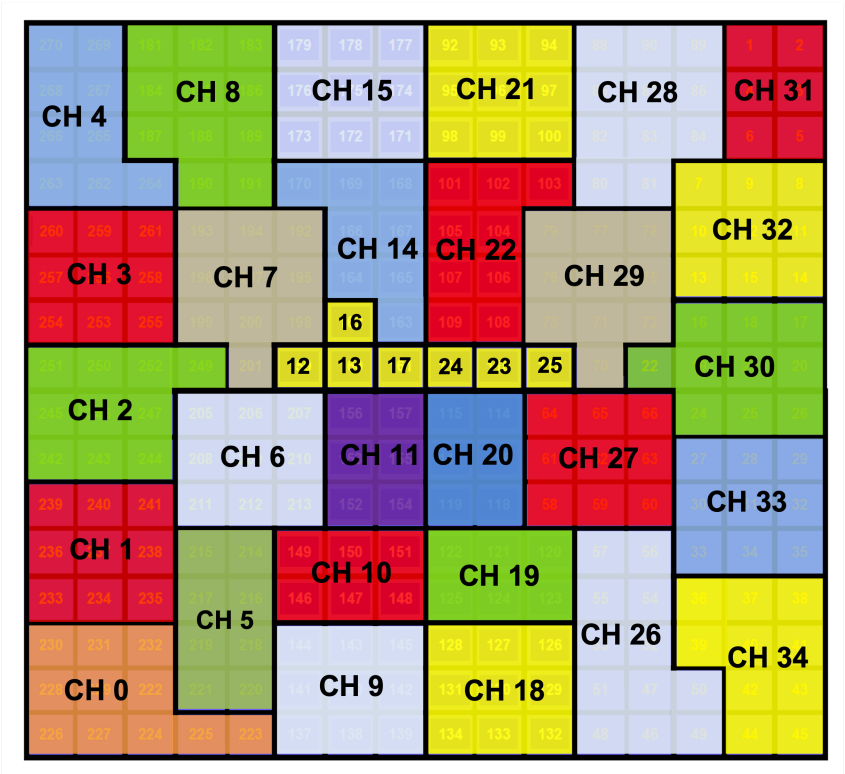


**Figure 1:** The pixel grouping used in iXRD.

# The iXRD

- Advantages of CdZnTe:
  - large band gap providing operation at room temperature
  - High stopping power due to large atomic number ($\sim$50)
  - High internal resistivity ($\sim 10^9 - 10^9 \Omega cm$)
- Disadvantages of CdZnTe:
  - Hole trapping effect
  - Expensive

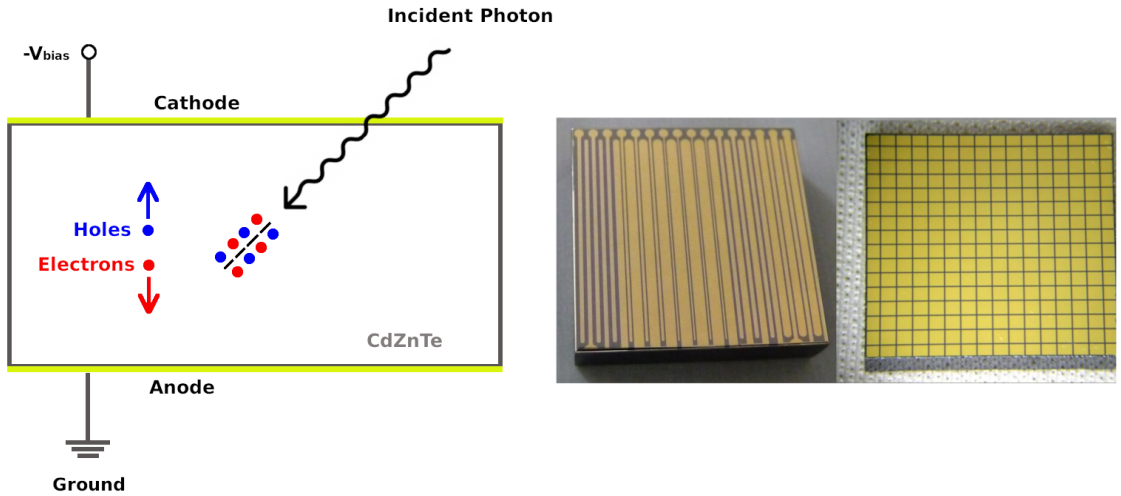


**Figure 2:** Left: Principle of charge carrier transportation and the charge induction on electrodes in CdZnTe detectors. Right: The two prominent electrode configuration for CdZnTe Detectors.

# Calibrations

- Calibration to obtain photon energies from the ADC levels.
- Two radioactive sources, $^{241}$Am (59.5 keV) and $^{57}$Co (122.1 keV, 136.5 keV).
- Pulser to determine the electronic noise and the intrinsic energy resolution for each channel.

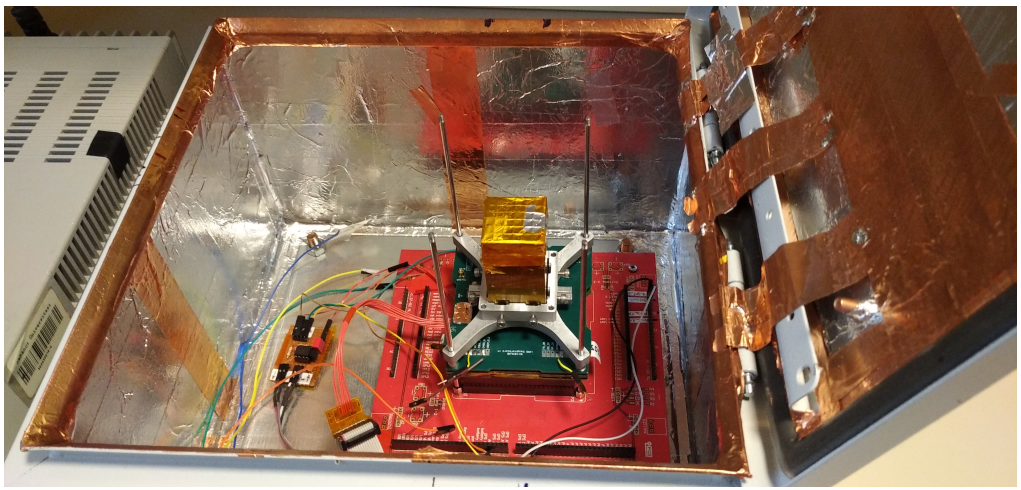

**Figure 3:** The calibration setup.

# Calibrations

- Calibration performed by fitting Gaussian functions to the 59.5 keV and 122.1 keV peaks from $^{241}$Am and $^{57}$Co sources, respectively.
- A linear fit performed to find the calibration parameters to go from the ADC channels to energy.
- Energy resolution calculated from the FWHM of the Gaussian peaks.

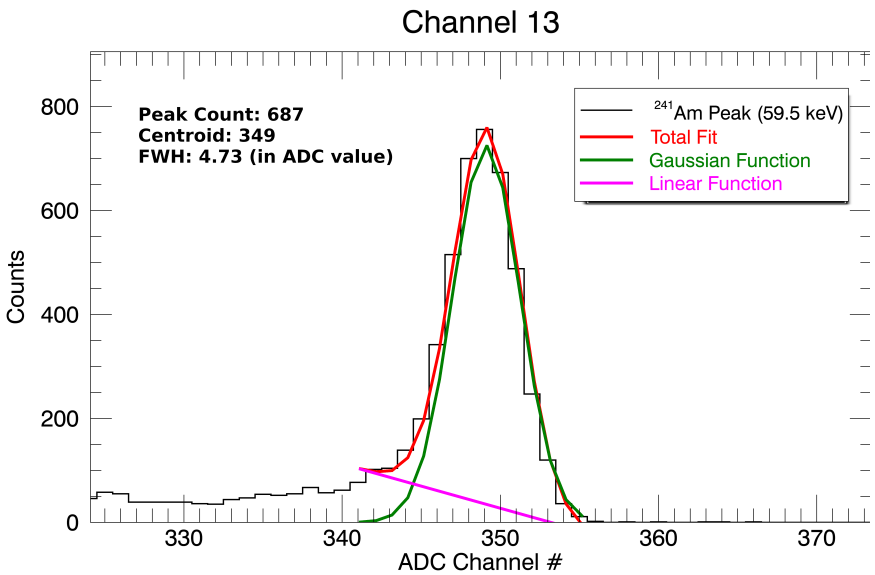


**Figure 4:** $^{241}$Am spectrum and illustration of the corresponding fit models for the channel 13.

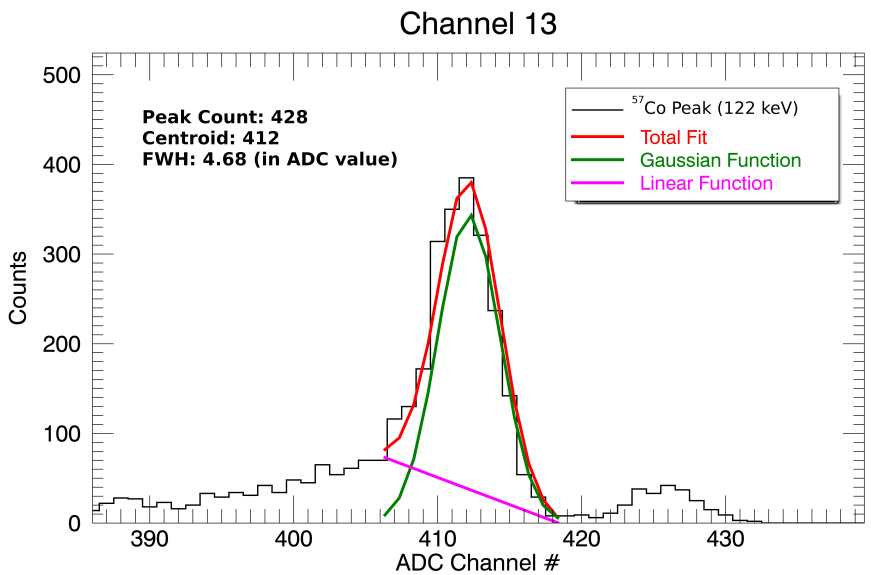


**Figure 5:** $^{57}$Co spectrum and illustration of the corresponding fit models for the channel 13.

# Calibrations

- The typical calibrated spectra for different pixel sizes.

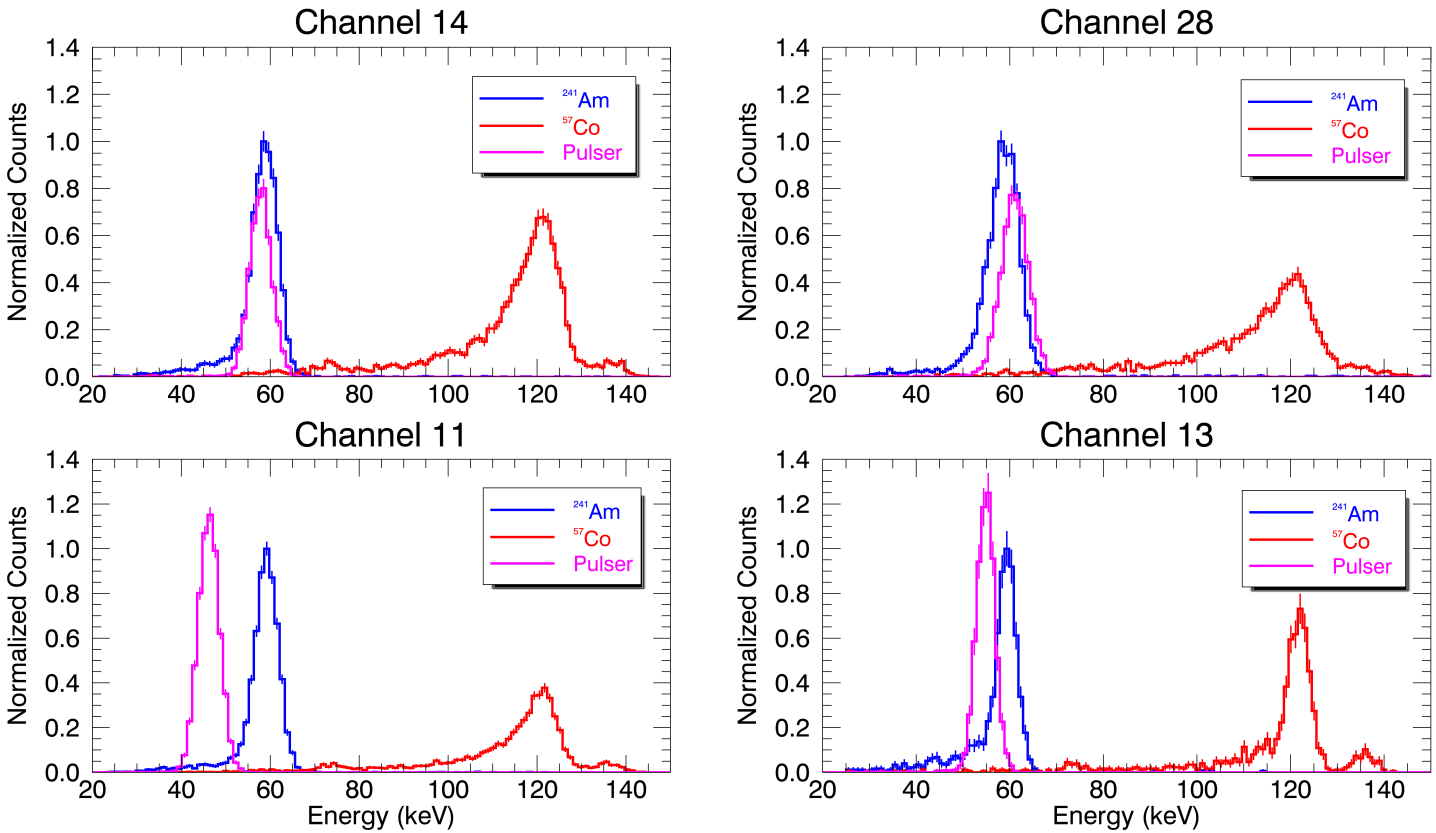


**Figure 6:** The energy spectra for Ch13 (single), Ch11 (small, 6 pixel), Ch14 (medium, 9 pixel), and Ch28 (large, 11 pixel). The results from the $^{57}$Co source are normalized by using the $^{241}$Am peak counts.

# Spectral performance of the iXRD

- Intrinsic FWHM 2.23, 2.93, 3.41, and 4.03 keV for single, small, medium, and large pixel groups respectively at 60 keV

**Table 1:** Energy resolution and minimum detectable energy values for each channel group averaged over the number of channels. The errors in FWHM calculations are less than 0.5%.

| Group Name | Channel Numbers | Pulser FWHM (keV) | $^{241}$Am FWHM (keV) | $^{57}$Co FWHM (keV) | Minimum Detectable Energy (keV) |
|---|---|---|---|---|---|
| Single | 12, 13, 16, 17, 23, 24, 25 | 3.787 ± 0.009 | 4.394 ± 0.005 | 4.325 ± 0.007 | 19.2 |
| Small | 10, 11, 19, 20, 31 | 3.883 ± 0.007 | 4.856 ± 0.007 | 7.149 ± 0.013 | 19.48 |
| Medium | 1, 3, 4, 5, 6, 9, 14, 15, 18, 21, 22, 27, 32, 33 | 5.576 ± 0.026 | 6.534 ± 0.009 | 9.380 ± 0.025 | 22.67 |
| Large | 0, 2, 7, 8, 26, 28, 29, 30, 34 | 5.973 ± 0.018 | 7.055 ± 0.008 | 10.592 ± 0.018 | 23.56 |

# Geant4 Simulation toolkit

- Geant4, a C++ based toolkit for Monte Carlo simulation of particles and radiation interacting with matter [3]

  - Physics processes including electromagnetic, hadronic and optical processes over a wide energy range from 250 eV to TeV

  - A detector simulation in Geant4:
    * Definitions of geometries, materials
    * Definitions of particles and relevant physics processes
    * Determination of source properties
    * Energy deposition in sensitive detector components
    * Storage of event and track info
    * Visualization of detector and particle trajectories

- Cosmic Diffuse X/$\gamma$-Rays (CDGRs)
  - Galactic and extra-galactic origins

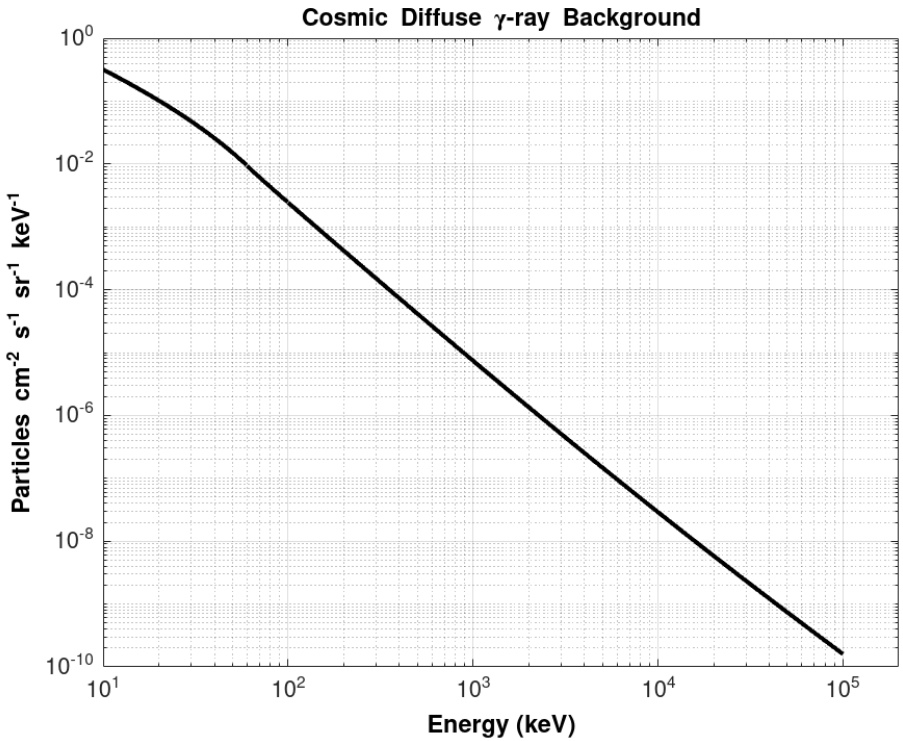


**Figure 7:** CDGRs (10 keV - 100 MeV) differential spectrum implemented in this work[4].

- Trapped Particles

  - Trapped electrons and protons coming from the Sun and the outer space by Earth's magnetic field.

  - SPENVIS (Space Environment Information System) [5] employed for the trapped particle models.

**Figure 8:** Representation of the composite motion of charged particles trapped in the Earth's magnetic field.[1]

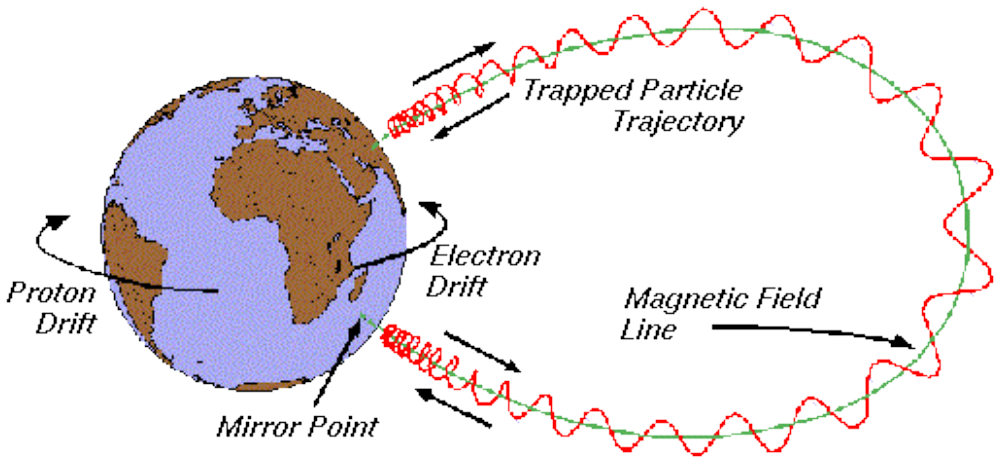


[1] https://www.SPENVIS.oma.be/help/background/traprad/traprad.html

- SPENVIS - Trapped Particles
  - Provides tools to simulate the satellite trajectory for given orbital parameters.

| Mission overview |
| --- |
| Orbit around: Earth |
| Number of mission segments: 1 |
| Mission start: 01/09/2022 00:00:00 |
| Mission end: 01/09/2023 00:00:00 |
| Mission duration: 365.00 days ( 1.00 years) |
| Satellite axis: zenith pointing |
| Orbit type: heliosynchronous |
| Apogee: 550.00 km |
| Perigee: 550.00 km |
| Inclination: 97.59° |
| R. A. Ascending Node: 339.76° |

**Figure 9:** Orbital parameters.

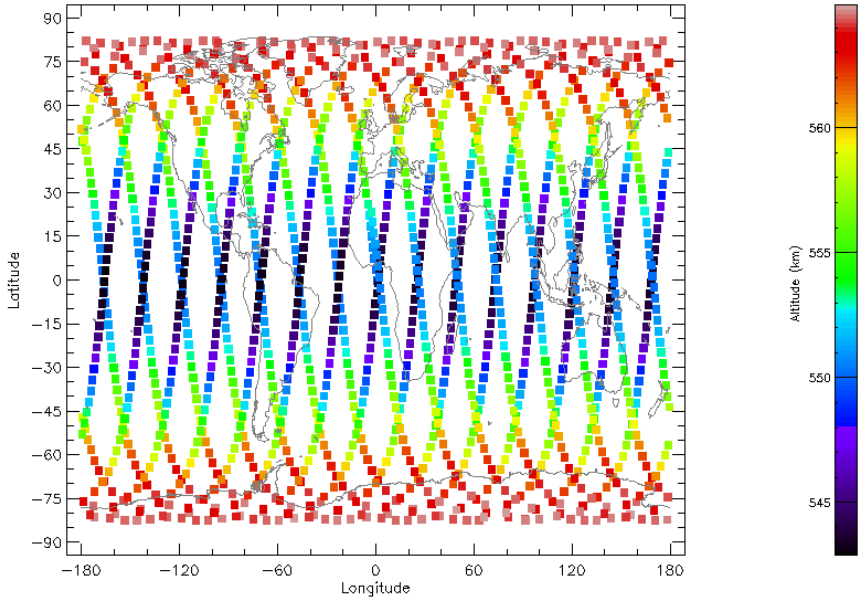


**Figure 10:** Altitude information as a function of longitude and latitude. Color bar indicates the altitude of the satellite.

- SPENVIS - Trapped Particles
  - Provides information on the trapped particle populations for the different dynamics such as solar cycles, the SAA region etc, along the orbital path.

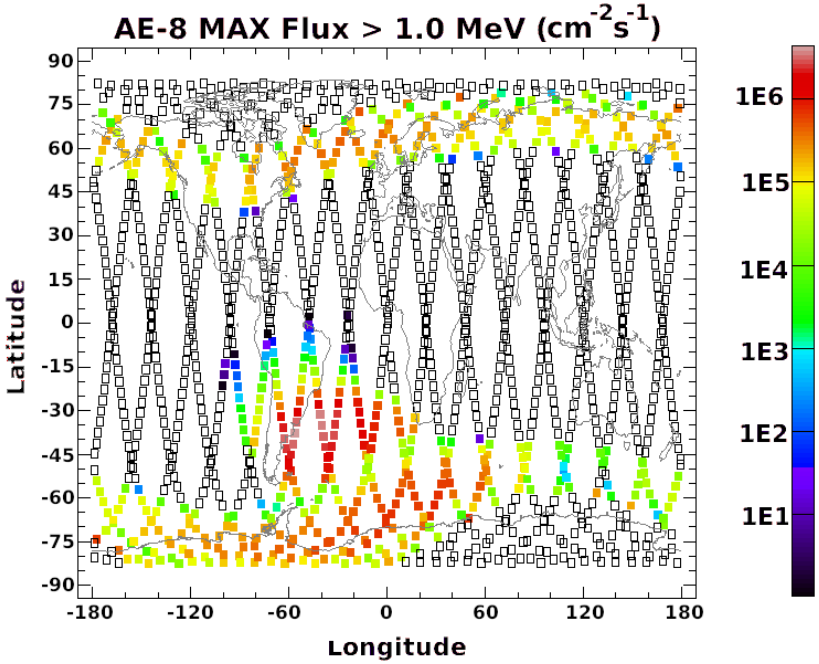


**Figure 11:** The average trapped electron flux to which SharjahSat-1 is exposed during one-day orbital trajectory.

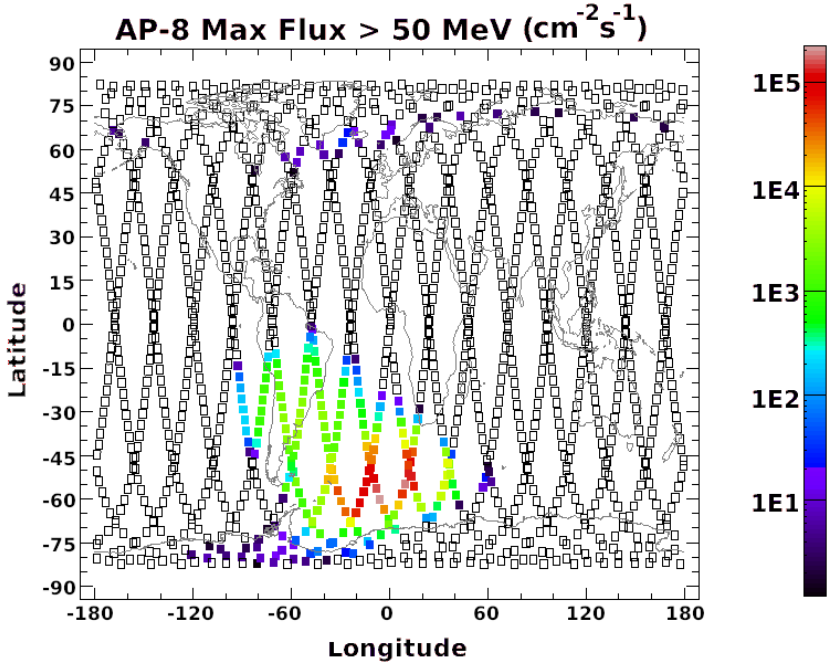


**Figure 12:** The trapped proton flux to which SharjahSat-1 is exposed during one-day orbital trajectory.

- SPENVIS - Trapped Particles

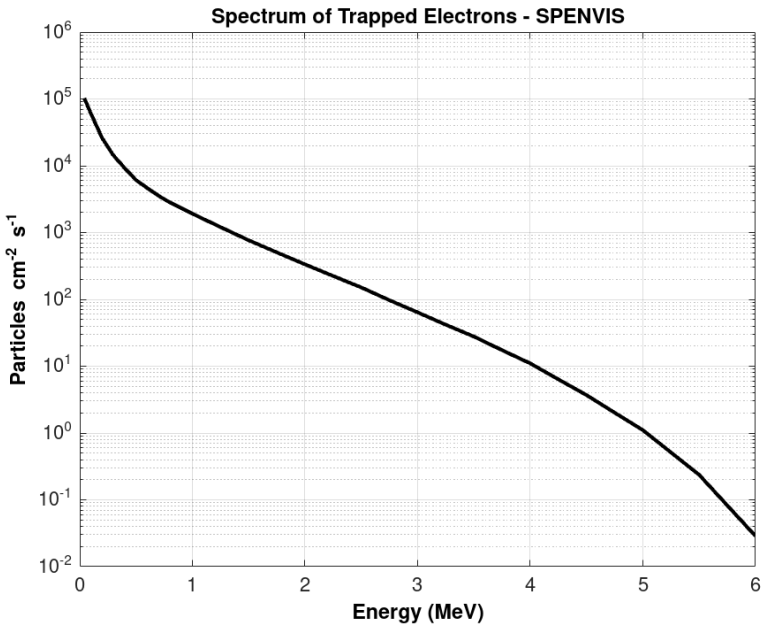


**Figure 13:** The average trapped electrons (40 keV - 6 MeV) integral spectrum.

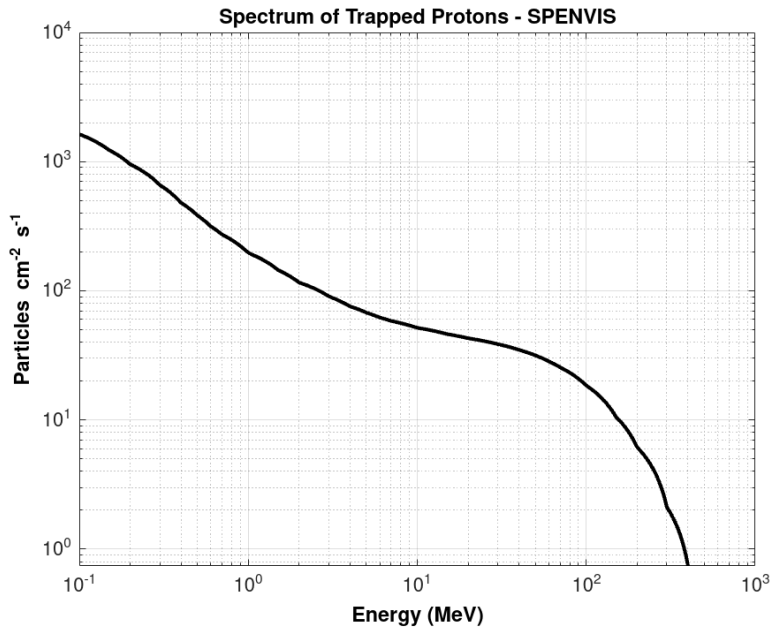


**Figure 14:** The average trapped protons (100 keV - 400 MeV) integral spectrum.

- SPENVIS - Galactic cosmic rays (GCRs)
  - Originating from the outside of the Solar System

~98% energetic, ionized nuclei from H to U, ~2% $e^-$ and $e^+$.
~87% hydrogen, ~12% helium, and ~1% heavier nuclei [6]

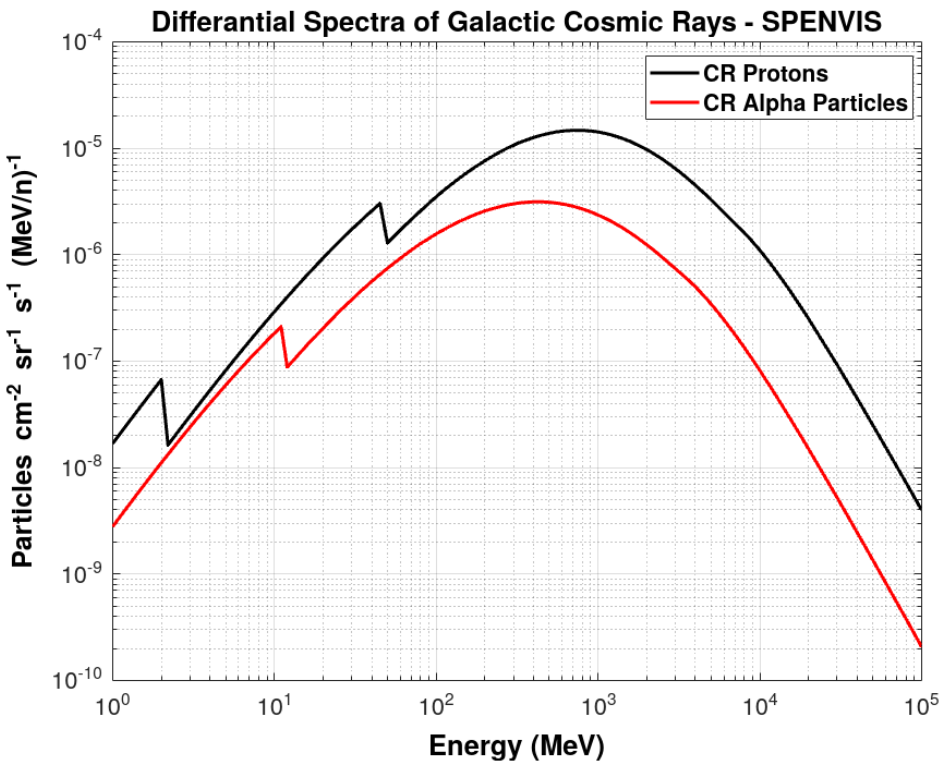


**Figure 15:** GCRs H and He ions (1 MeV - 100 GeV) differential spectrum implemented in this work.

- Albedo Photons
  - Radiation from outer layers of the Earth's atmosphere, due to the cosmic rays interactions with the atmosphere, as well as the reflection of the CDGR from the atmosphere.

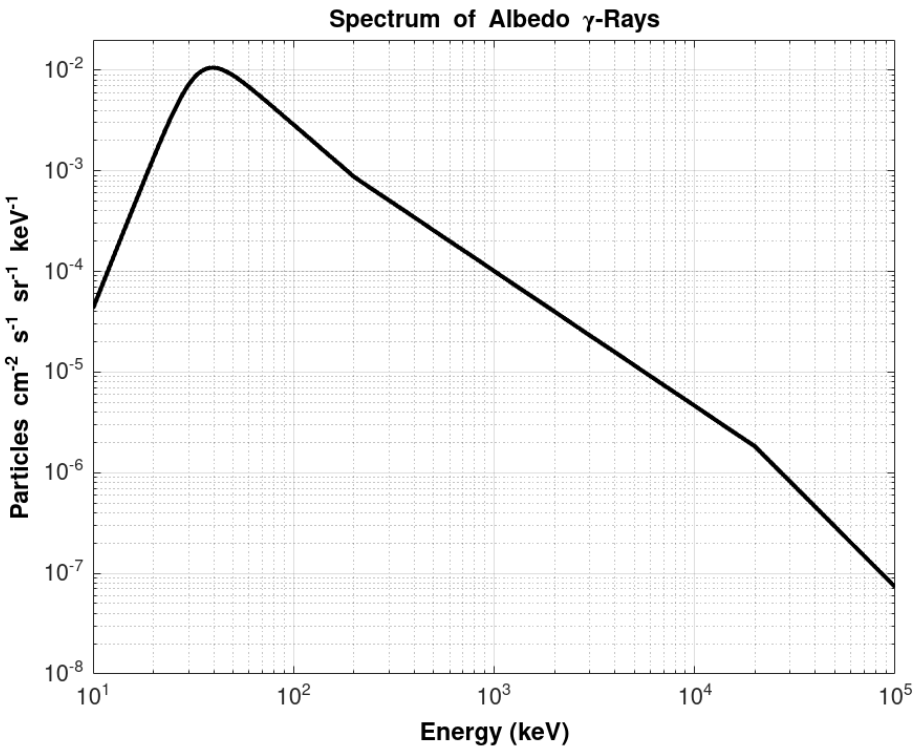


**Figure 16:** Albedo photons (10 keV - 100 MeV) differential spectrum implemented in this work[7].

- Albedo Neutrons
  - Neutron emission from the atmosphere due to bombardment of cosmic rays on the atmospheric nuclei.

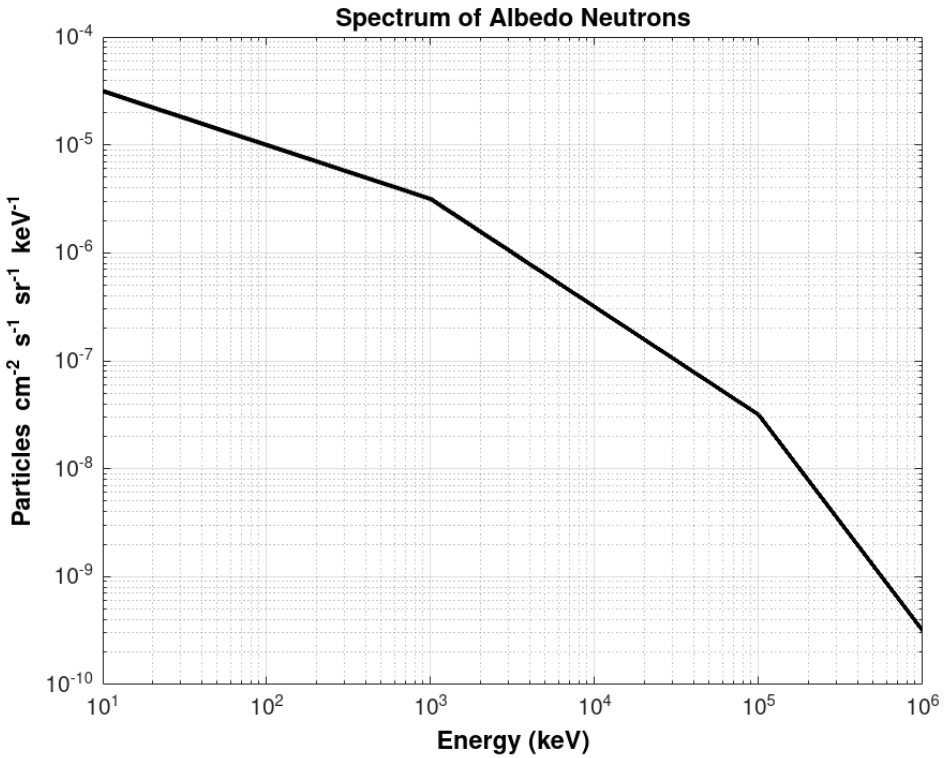


**Figure 17:** Albedo neutrons (10 keV - 1 GeV) differential spectrum implemented in this work[7].

# Background Radiation Simulations

- SharjahSat-1 mass model in Geant4 including all important geometries such as the iXRD system, PCBs, aluminum shielding boxes for the electronic components, batteries, and all structural supports etc.

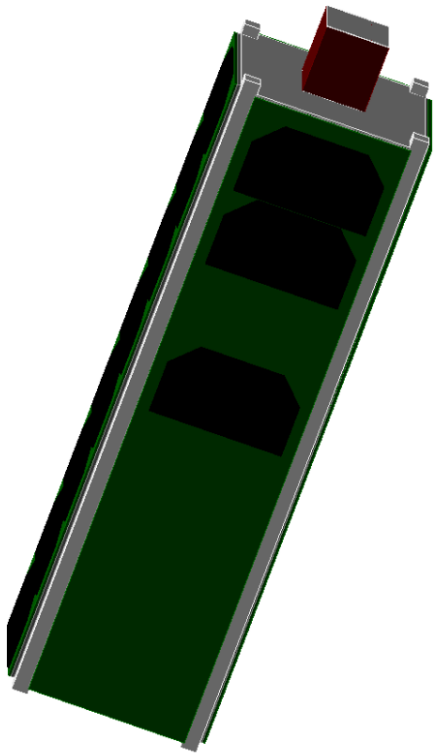

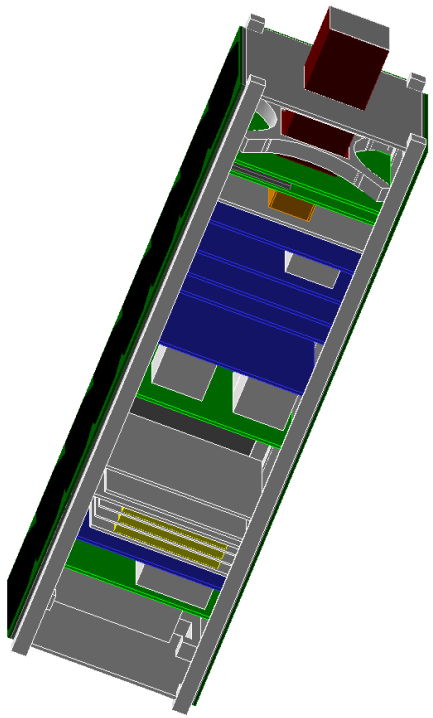

# Background Radiation Simulations

- The Shielding Physics List used:
  - packages for electromagnetic and hadronic physics processes.
- The spectral models for background radiation given as inputs in Geant4.
- A virtual sphere with 90 cm radius surrounding the cubesat created, source particle positions and angular distributions randomly created by Geant4.
  - Source particles radiated inward towards the satellite.

# Background Radiation Simulations

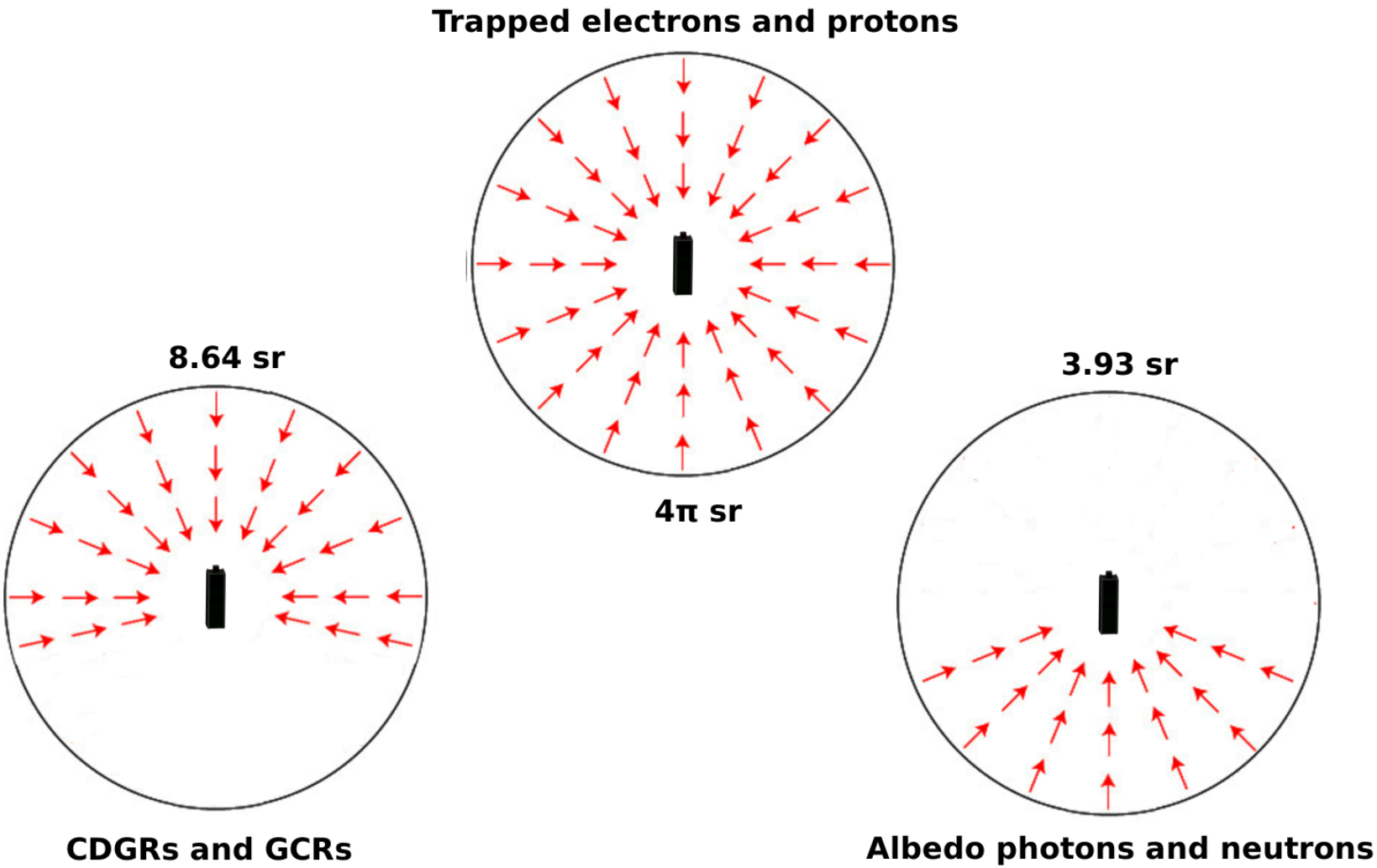

# Background Radiation Simulations

- The spectral models for background radiation given as inputs in Geant4.
- The spectra divided into bins equal in logarithmic scale.
  - For instance, albedo photon spectrum divided into 500 bins, 500 separate simulations injecting $10^5$ primary photons per bin

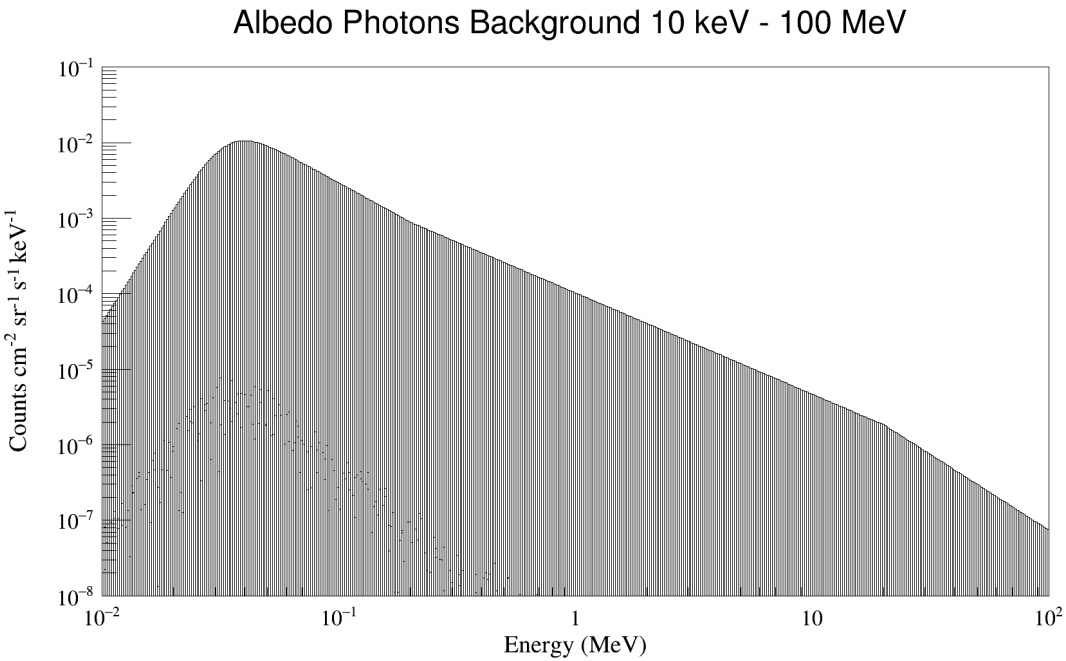

# Trapped Particle Count Rates

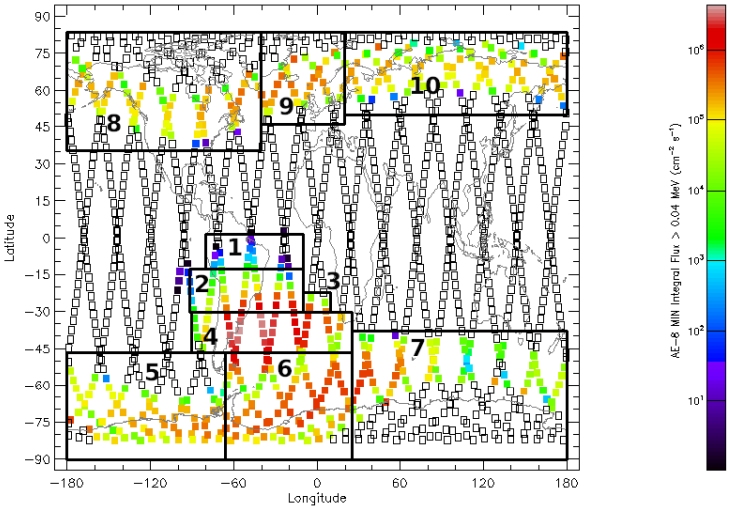


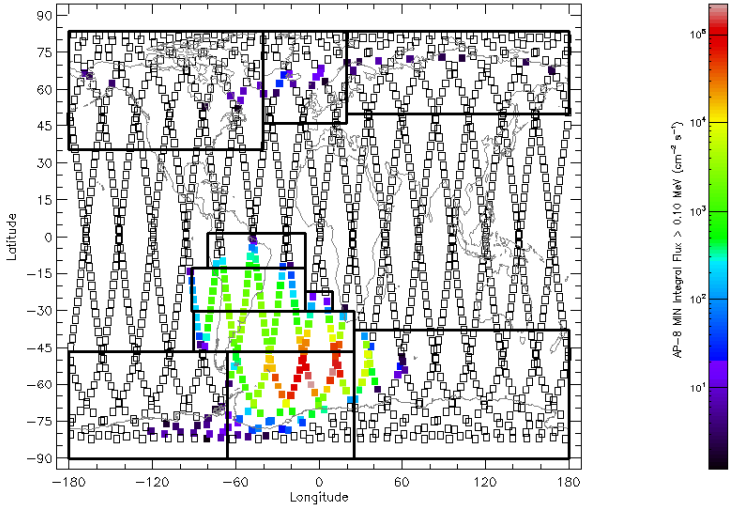


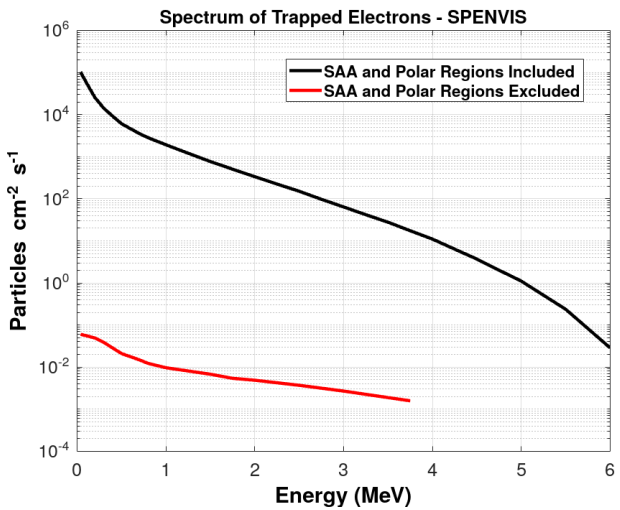


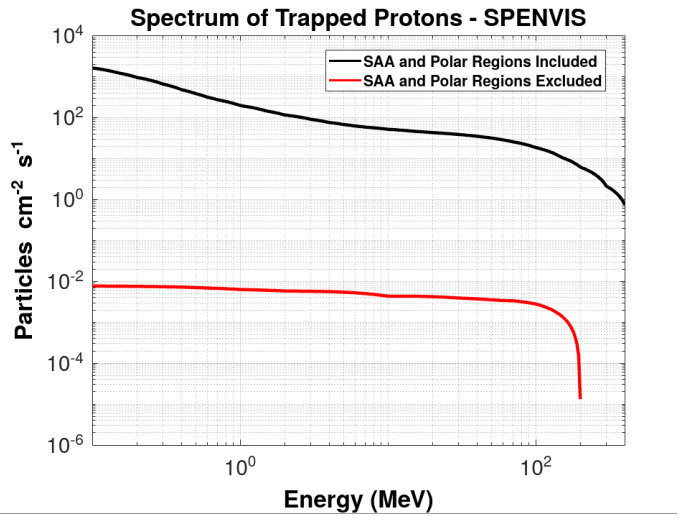

# Trapped Particle Count Rates

**Table 2:** The background count rates for the trapped particles in the orbit inside and outside of the SAA and the polar regions. The count rates are calculated for the particles that deposit energy greater than 20 keV in the detector volume.

| **Region** | **Trapped** $p^+$ (0.1-400 MeV) (cnt/s) | **Trapped** $e^-$ (0.04-7 MeV) (cnt/s) |
|---|---|---|
| Including the SAA and Polar Regions | 9047.7 | 1240.0 |
| Excluding the SAA and Polar Regions | 1.01 | 0.01 |

# Total background spectrum and count rates

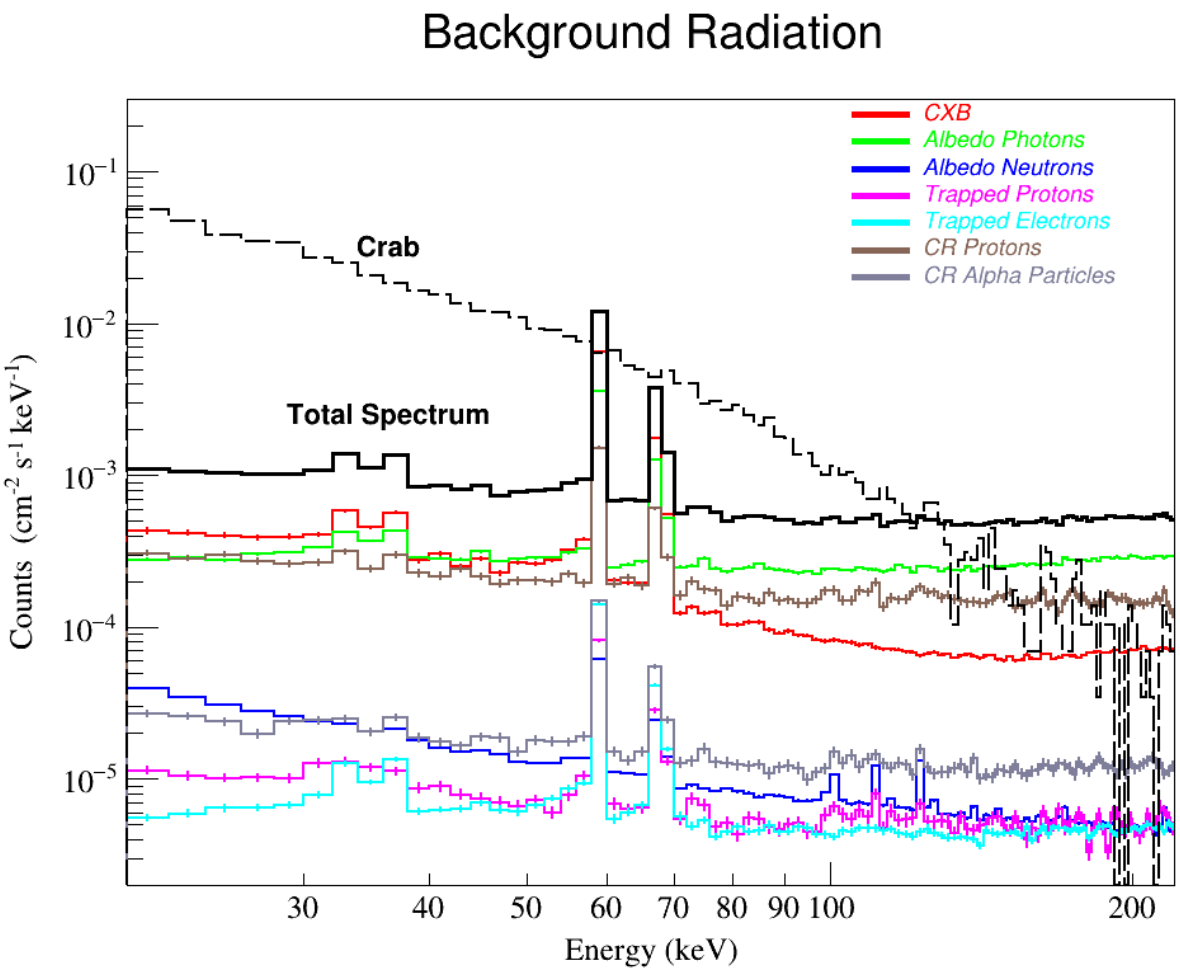


**Figure 18:** Spectra of the background radiation components obtained with the help of the deposited energies of the background particles in the crystal calculated by Geant4 simulations. The total background is shown and labeled in black color. Crab spectrum is also included in the plot and labeled in black color.

# Simulations for Detector Spectral Response

- A C++ code (called THEBES - Transporter of Holes and Electrons By Electric field in Semiconductor Detectors) for transportation of charge clouds and charge induction on the electrodes

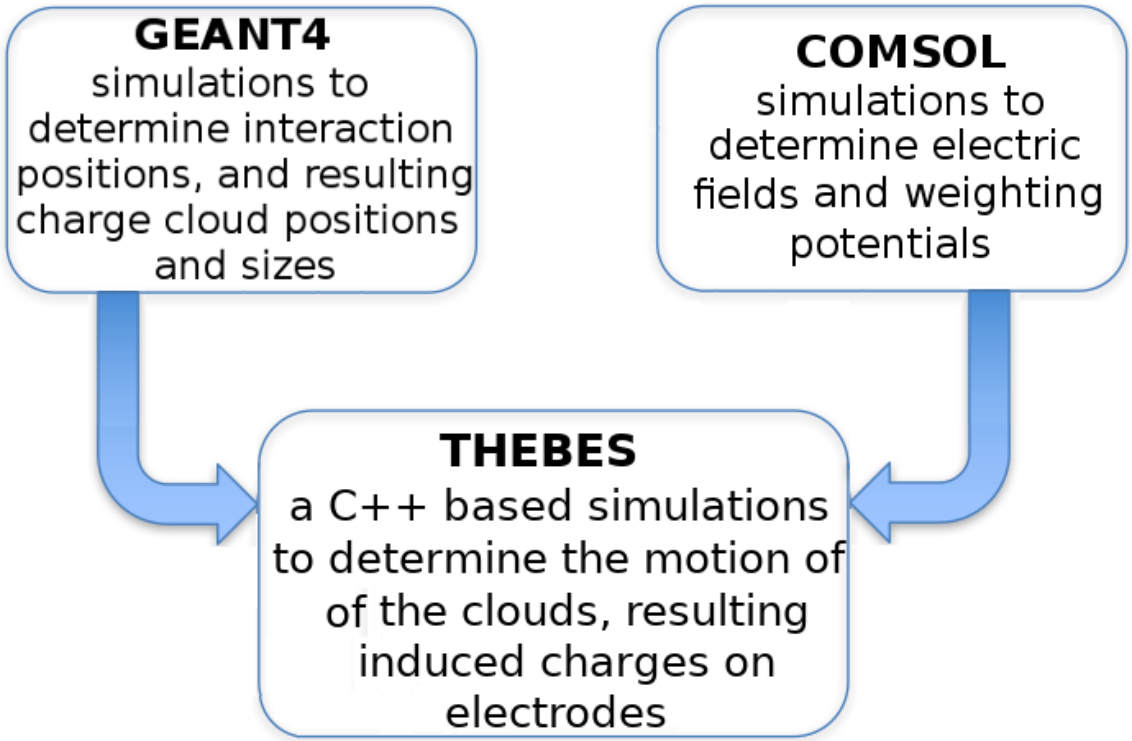


**Figure 19:** Simulation framework.

# Comsol Simulations

- COMSOL Multiphysics software to model:
  - Electric fields
  - Weighting potential distributions in the crystal volume [8]
  - $Q_{ind}(x) = - q \times w(x)$

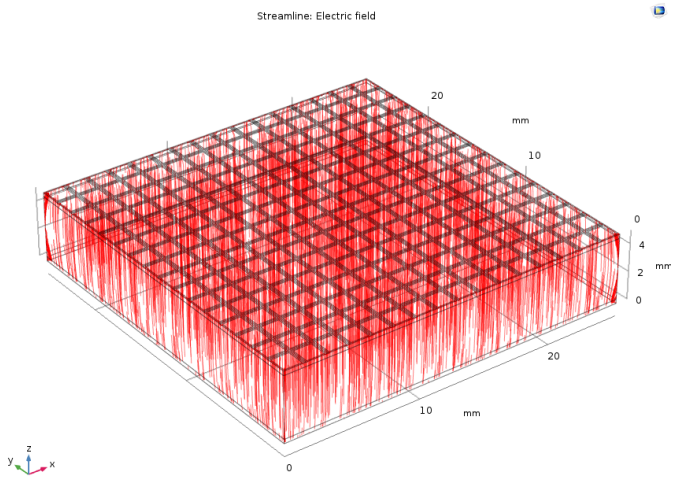


**Figure 20:** Illustration of the electric field lines in Comsol software.

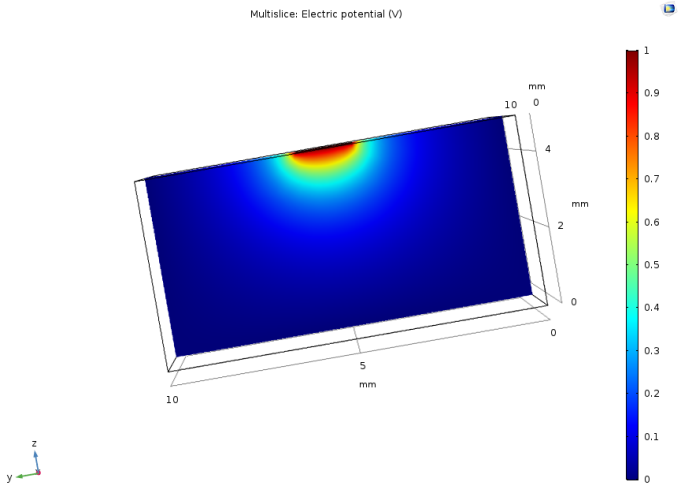


**Figure 21:** Illustration of the weighting potential distribution of a single electrode.

# THEBES simulation

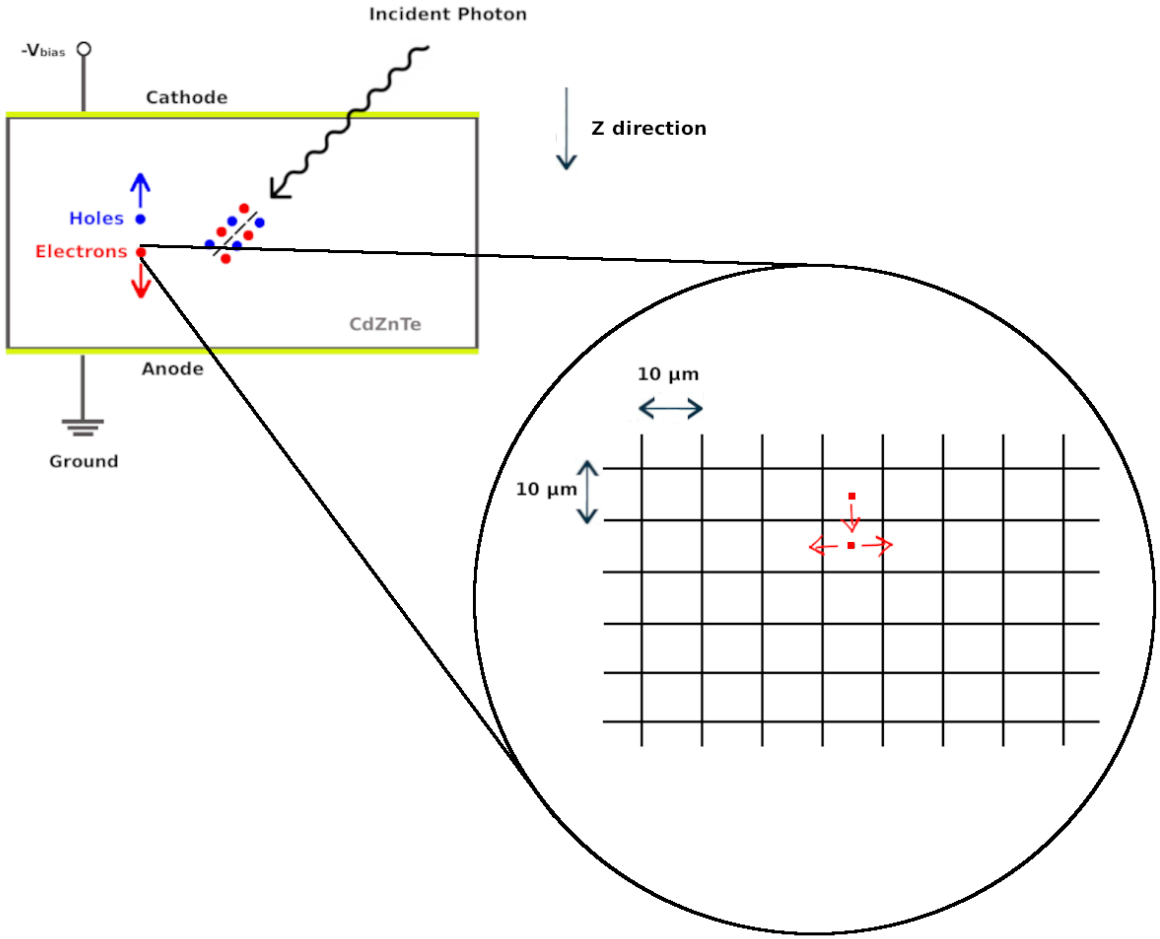

# THEBES simulation

- Electron cloud expansion due to diffusion and electrostatic repulsion.

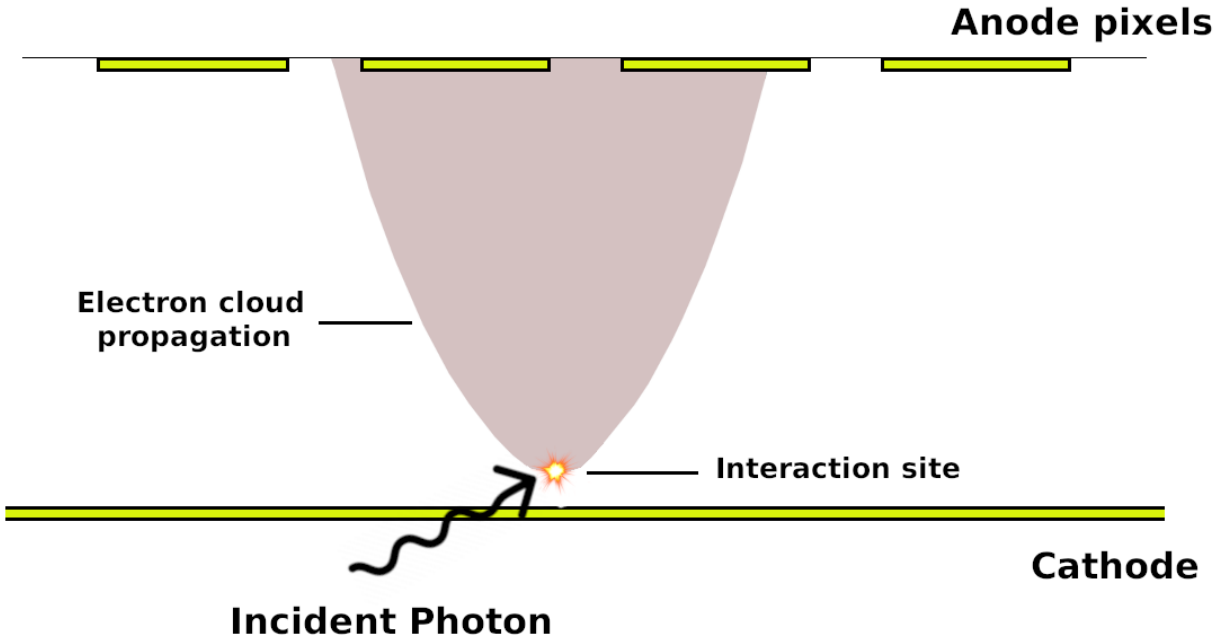


**Figure 22:** Illustration of electron cloud expansion during the drift toward anode pixels.

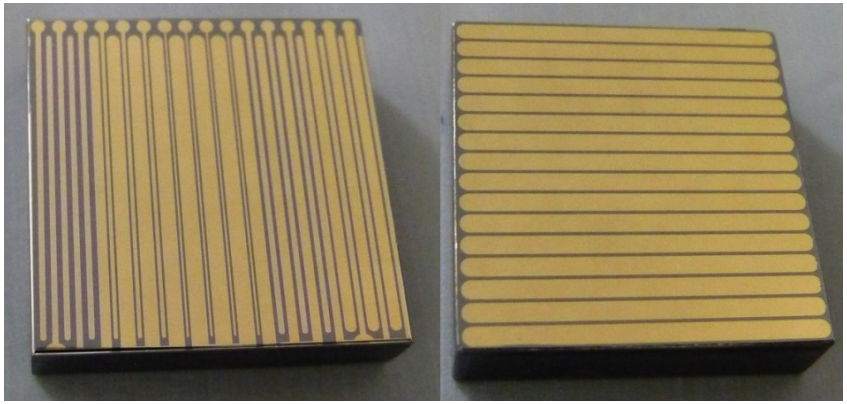

**Figure 23:** Picture of the CdZnTe crystal with cross-strip electrode geometry.

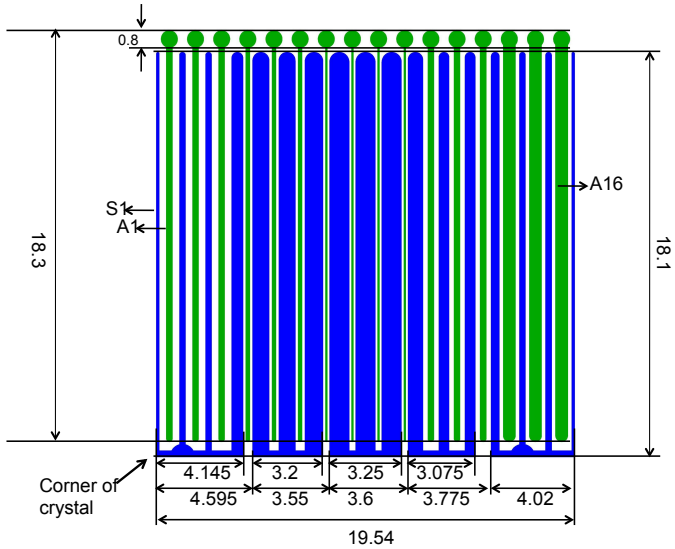


**Figure 24:** Drawing of the anode/SE side. Green strips represent the anodes, while the blue ones are for the SE strips. Pitch is constant at 1.2 mm. All measurements are in mm.

# THEBES simulation

- Our findings published in Nuclear Inst. and Methods in Physics Research, A", `https://doi.org/10.1016/j.nima.2021.166125`

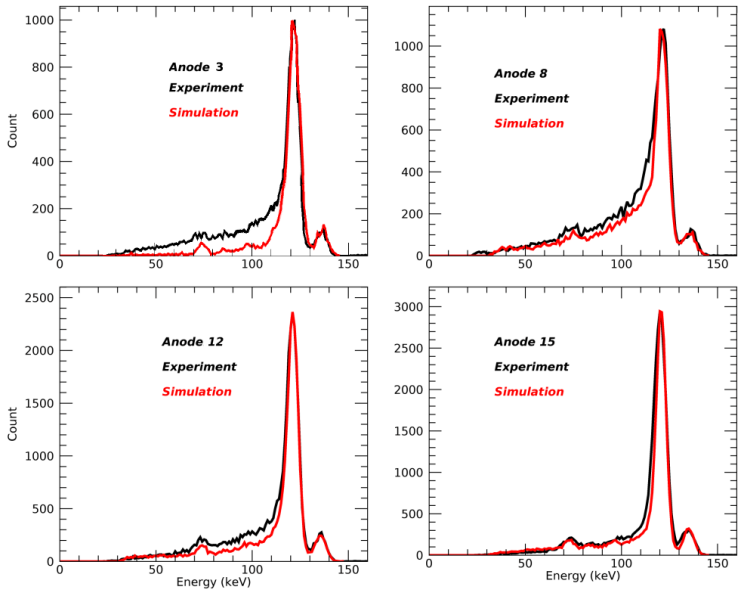


**Figure 25:** Comparison of experimental and simulation results. Anodes numbered 3, 8, 12, and 15 are used. The simulation results are normalized by using the peak counts from the experiment spectra for the comparative purpose.

# iXRD Sensitivity Estimations

- Sensitivity defined as the limiting intensity of the detector for a weak source observation at a particular significance level

$$F_{min} = SNR \cdot \frac{\sqrt{2.33 \cdot B(E)}}{f_{live} \cdot A_{eff}(E) \cdot \sqrt{T} \cdot \sqrt{FWHM(E)}}$$

- $F_{min}$ is the sensitivity of the iXRD at a given energy E
- SNR is the signal-to-noise ratio
- $B$ is the simulated background radiation counts $cm^{-2}$ $s^{-1}$ $keV^{-1}$ at a given energy $E$
- $f_{live}$ is the livetime fraction
- $A_{eff}$ is the effective area of the iXRD at a given energy $E$
- $T$ is the total observing time
- $FWHM$ is the full width at maximum for the energy resolution of the iXRD at a given energy $E$

# iXRD Sensitivity Estimations

- Background simulation of 9000 seconds of integration time (indicating one day), due to the 600 seconds operation time of the iXRD in each orbit.
- THEBES simulations by making use of the Geant4 background simulation outputs as input

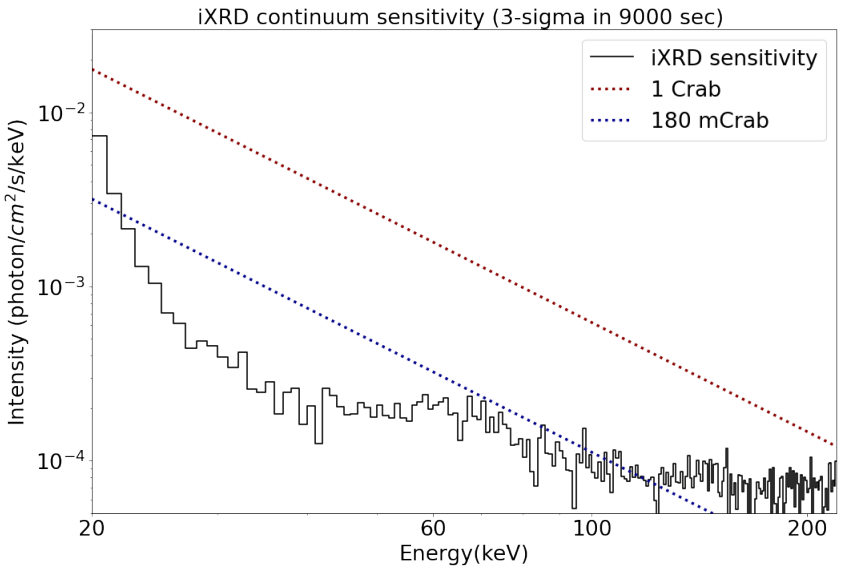


**Figure 26:** Simulated sensitivity curve of iXRD with observation time of 9000 seconds, livetime fraction of 90% and SNR of 3

# iXRD Sensitivity Estimations

- Continuum sensitivity of the iXRD is about 180 mCrab ($\sim$0.07 photons $cm^{-2}$ $s^{-1}$) between 20 to 100 keV energy band.
- The Sco X-1 corresponds to $\sim$0.24 photons $cm^{-2}$ $s^{-1}$ in the energy range of 20 keV - 50 keV [11], [12], while the ixrd sensitivity 0.05 photons $cm^{-2}$ $s^{-1}$.
- the Cygnus X-1 observed at a flux level of approximately $\sim$0.29 photons $cm^{-2}$ $s^{-1}$ between the energies 20 keV and 120 keV [14]

# Conclusion

- We developed a hard X-ray detector as a scientific payload of SharjahCubeSat-1.
- The first satellite with scientific mission developed in Turkey.
- The iXRD energy resolution of 4-5 keV at 60 keV
- Background radiation simulation indicates that the dominant background components: CDGR, Albedo photons and GC protons.
- THEBES simulations to obtained the spectral response of the iXRD enables to calculate estimated sensitivity of the iXRD which is $\sim$0.07 photons $cm^{-2}$ $s^{-1}$
- The experience gained during the iXRD development may provide significant contributions for the prospective future projects.
- Possible improvements on the system, in terms of using an ASIC with better properties, electrode configuration, utilizing scintillation veto detectors to discard background signals.

# Publications


- Altıngün, A.M., Kalemci, E.: Optimization study of the electrode design of a 5 mm thick orthogonal-strip CdZnTe detector system. Nuclear Instruments and Methods in Physics Research, Section A: Accelerators, Spectrometers, Detectors and Associated Equipment 1027(December 2020), 166125 (2022). https://doi.org/10.1016/j.nima.2021.166125
- Altıngün, A.M., Kalemci, E.: A simulation study for the expected performance of sharjahsat-1 payload improved x-ray detector (iXRD) in the orbital background radiation. submitted to Experimental Astronomy (2022)
- Kalemci, E., Altıngün, A.M., Bozkurt, A., Aslan, A.R., Yalçın, R., Gökalp, K., Veziroğlu, K., Fernini, I., Manousakis, A., Yaşar, A., Diba, M., Karabulut, B., Çatal, E., Öztekin, O.: The improved x-ray detector (ixrd) on sharjah-sat-1, design principles, tests and ground calibration. submitted to Experimental Astronomy (2022)

# Publications


- Kalemci, E., Manousakis, A., Fernini, I., Al Naimiy, H., Bozkurt, A., Aslan, A.R., Altıngün, A.M., Veziroğlu, K., Yalçın, R., Gökalp, K., Diba, M., Yaşar, A., Öztaban, E., Karabulut, B., Öztekin, O., Farouk, Y., Alsabt, I., AlKaabi, T., Shaikh, M.M., Madara, S.R.: Scientific contribution of sharjah-sat-1 to x-ray observations. In: IAC 2021 Congress Proceedings, 72nd International Astronautical Congress (IAC), Dubai, United Arab Emirates, p. 63844 (2021). IAF
- Faroukh, Y., Alkaabi, T., Kalemci, E., Al-Sabt, I., BinAshour, M., Altıngün, M.A., Gökalp, K., Yalçın, R., Alketbi, F., Alhammadi, A., Alansaari, M., Karabulut, B., Catal, E., Fernini, I., Aslan, A.R., Al-Naimiy, H.M.K.: Design, testing, and validation of a space-based

*Thank You*

[1] E. Kalemci, E. Ümit, and R. Aslan, "X-ray detector on 2u cubesat beeaglesat of qb50," in *2013 6th International Conference on Recent Advances in Space Technologies (RAST)*, pp. 899–902, 2013.

[2] G. F. Knoll, *Radiation detection and measurement / Glenn F. Knoll.*
Wiley New York, 2nd ed. ed., 1989.

[3] S. Agostinelli, J. Allison, K. Amako, J. Apostolakis, H. Araujo, P. Arce, M. Asai, D. Axen, S. Banerjee, G. Barrand, F. Behner, L. Bellagamba, J. Boudreau, L. Broglia, A. Brunengo, H. Burkhardt, S. Chauvie, J. Chuma, R. Chytracek, G. Cooperman, G. Cosmo, P. Degtyarenko, A. Dell'Acqua, G. Depaola, D. Dietrich, R. Enami, A. Feliciello, C. Ferguson, H. Fesefeldt, G. Folger, F. Foppiano, A. Forti, S. Garelli, S. Giani, R. Giannitrapani, D. Gibin, J. Gómez Cadenas, I. González, G. Gracia Abril,

G. Greeniaus, W. Greiner, V. Grichine, A. Grossheim,
S. Guatelli, P. Gumplinger, R. Hamatsu, K. Hashimoto,
H. Hasui, A. Heikkinen, A. Howard, V. Ivanchenko,
A. Johnson, F. Jones, J. Kallenbach, N. Kanaya,
M. Kawabata, Y. Kawabata, M. Kawaguti, S. Kelner, P. Kent,
A. Kimura, T. Kodama, R. Kokoulin, M. Kossov,
H. Kurashige, E. Lamanna, T. Lampén, V. Lara, V. Lefebure,
F. Lei, M. Liendl, W. Lockman, F. Longo, S. Magni,
M. Maire, E. Medernach, K. Minamimoto, P. Mora de Freitas,
Y. Morita, K. Murakami, M. Nagamatu, R. Nartallo,
P. Nieminen, T. Nishimura, K. Ohtsubo, M. Okamura,
S. O'Neale, Y. Oohata, K. Paech, J. Perl, A. Pfeiffer, M. Pia,
F. Ranjard, A. Rybin, S. Sadilov, E. Di Salvo, G. Santin,
T. Sasaki, N. Savvas, Y. Sawada, S. Scherer, S. Sei,
V. Sirotenko, D. Smith, N. Starkov, H. Stoecker, J. Sulkimo,
M. Takahata, S. Tanaka, E. Tcherniaev, E. Safai Tehrani,
M. Tropeano, P. Truscott, H. Uno, L. Urban, P. Urban,

M. Verderi, A. Walkden, W. Wander, H. Weber, J. Wellisch, T. Wenaus, D. Williams, D. Wright, T. Yamada, H. Yoshida, and D. Zschiesche, "Geant4—a simulation toolkit," *Nuclear Instruments and Methods in Physics Research Section A: Accelerators, Spectrometers, Detectors and Associated Equipment*, vol. 506, no. 3, pp. 250–303, 2003.

[4] D. E. Gruber, J. L. Matteson, L. E. Peterson, and G. V. Jung, "The spectrum of diffuse cosmic hard x-rays measured with heao-1," *The Astrophysical Journal*, vol. 520, pp. 124–129, 1999.

[5] D. Heynderickx, B. Quaghebeur, J. Wera, E. J. Daly, and H. D. R. Evans, "New radiation environment and effects models in the european space agency's space environment information system (spenvis)," *Space Weather*, vol. 2, no. 10, p. S10S03, 2004.

[6] J. A. Simpson, "Elemental and isotopic composition of the galactic cosmic rays," *Annual Review of Nuclear and Particle Science*, vol. 33, no. 1, pp. 323–382, 1983.

[7] R. Sarkar, S. Mandal, D. Debnath, T. B. Kotoch, A. Nandi, A. R. Rao, and S. K. Chakrabarti, "Instruments of RT-2 experiment onboard CORONAS-PHOTON and their test and evaluation IV: Background simulations using GEANT-4 toolkit," *Experimental Astronomy*, vol. 29, no. 1, pp. 85–107, 2011.

[8] Z. He, "Review of the shockley–ramo theorem and its application in semiconductor gamma-ray detectors," *Nuclear Instruments and Methods in Physics Research Section A: Accelerators, Spectrometers, Detectors and Associated Equipment*, vol. 463, no. 1, pp. 250 – 267, 2001.

[9] E. Kalemci, J. L. Matteson, R. T. Skelton, P. L. Hink, and K. R. Slavis, "Model calculations of the response of CZT strip detectors," in *Hard X-Ray, Gamma-Ray, and Neutron Detector Physics* (R. B. James and R. C. Schirato, eds.), vol. 3768, pp. 360 – 373, International Society for Optics and Photonics, SPIE, 1999.

[10] M. Benoit and L. A. Hamel, "Simulation of charge collection processes in semiconductor CdZnTe $\gamma$-ray detectors," *Nuclear Instruments and Methods in Physics Research A*, vol. 606, pp. 508–516, July 2009.

[11] F. D. . Amico, W. A. Heindl, R. E. Rothschild, and D. E. Gruber, "HIGH-ENERGY X-RAY TIMING EXPERIMENT DETECTIONS OF HARD X-RAY TAILS IN SCORPIUS X-1," *The Astrophysical Journal*, vol. 547, pp. 147–150, 2001.

[12] R. K. Manchanda, "Hard X-ray component in Sco X-1 spectrum: Synchrotron emission from a nano quasar," *Advances in Space Research*, vol. 37, no. 11, pp. 2139–2145, 2006.

[13] R. K. Manchanda, "X-ray Measurements of Black Hole X-ray Binary Source GRS 1915+105 and the Evolution of Hard X-ray Spectrum," *J. Astrophys. Astr*, vol. 21, pp. 39–52, 2000.

[14] P. Ubertini, A. Bazzano, C. La Padula, R. K. Manchanda, V. F. Polcaro, R. Staubert, E. Kendziorra, and F. Perotti, "Low-Flux Hard X-Ray Observation of Cygnus X-1," *Astrophysical Journal*, vol. 383, p. 263, Dec. 1991.

[15] M. Xu, "Ritsumeikan beamer theme," in *How to write beautiful LaTeX*, 2022.

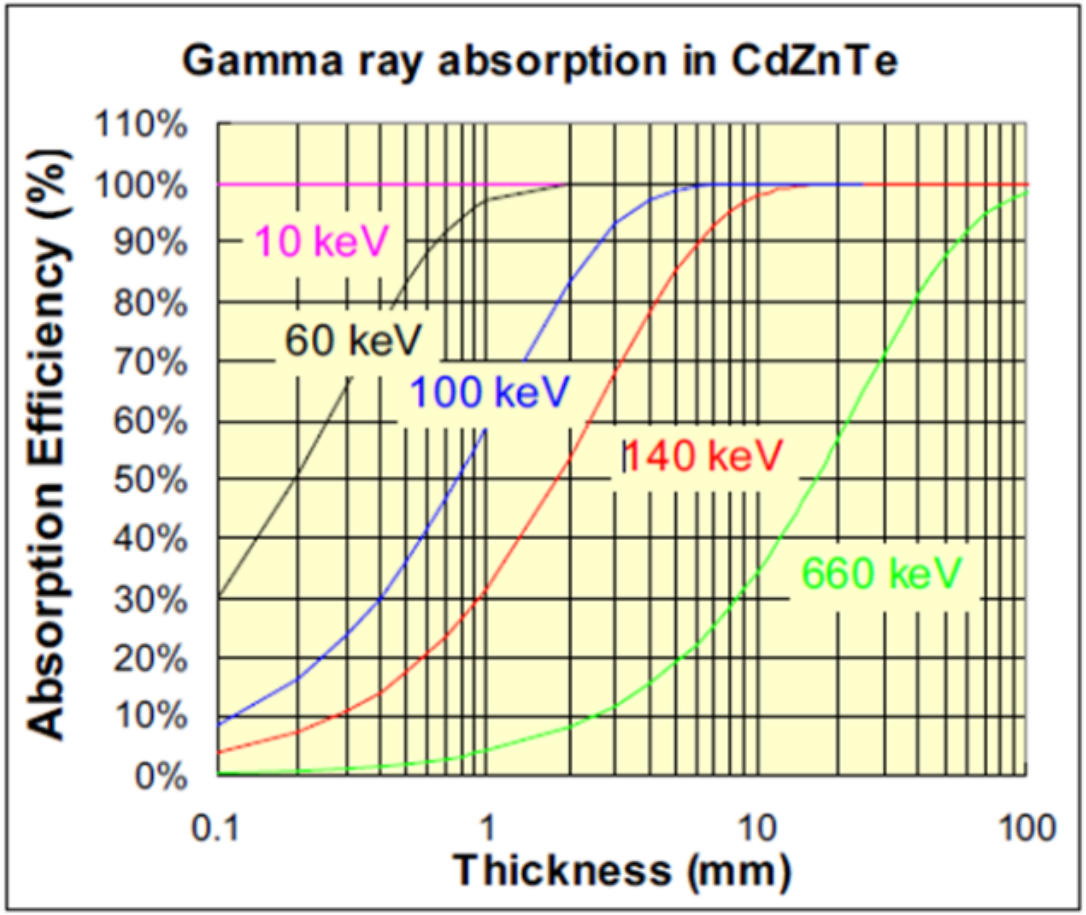



- Szeles, C. (2004), CdZnTe and CdTe materials for X-ray and gamma ray radiation detector applications. phys. stat. sol. (b), 241: 783-790. https://doi.org/10.1002/pssb.200304296

**Table 1.** Comparison of semiconductor materials for pixel detectors

| Material | Si[31] | Ge[31] | GaAs:Cr[32] | epi-GaAs[31] | CdTe[33] | $Cd_{0.9}Zn_{0.1}Te$[34] | TlBr[35] |
|---|---|---|---|---|---|---|---|
| Growth method [a)] | CZ | CZ | CZ | CVD | THM | THM | BM |
| Atomic number | 14 | 32 | 31, 33 | 31, 33 | 48, 52 | 48, 30, 52 | 81, 35 |
| Density [g $cm^{-3}$] | 2.33 | 5.33 | 5.32 | 5.32 | 5.85 | 5.78 | 7.56 |
| Band gap [eV] | 1.12 | 0.67 | 1.43 | 1.43 | 1.44 | 1.57 | 2.68 |
| Resistivity [Ω cm] | $10^4$ | 50 | $10^9$ | $10^7$ | $10^9$ | $10^{10}$ | $10^{12}$ |
| Pair creation energy [eV] | 3.62 | 2.96 | 4.2 | 4.2 | 4.43 | 4.6 | 6.5 |
| $\mu_e\tau_e$ [$cm^2$ $V^{-1}$] | >1 | >1 | $10^{-5}$ | $10^{-6}$ | $10^{-3}$ | $10^{-1}$ | $10^{-4}$ |
| $\mu_h\tau_h$ [$cm^2$ $V^{-1}$] | 1 | >1 | $10^{-6}$ | $10^{-6}$ | $10^{-4}$ | $10^{-5}$ | $10^{-5}$ |

[a] The growth methods are: CZ: Czochralski (liquid encapsulated for GaAs); CVD = chemical vapor deposition; THM = travelling heater method using tellurium solution; BM = Bridgman method. The data were collected from Del Sordo,[31] Veale,[32] Toyokawa,[33] Zappettini,[34] and Nogami.[35]

- Fiederle, M., Procz, S., Hamann, E., Fauler, A., Fröjdh, C., Overview of GaAs und CdTe Pixel Detectors Using Medipix Electronics. Crystal Research and Technology 2020, 55, 2000021. https://doi.org/10.1002/crat.202000021

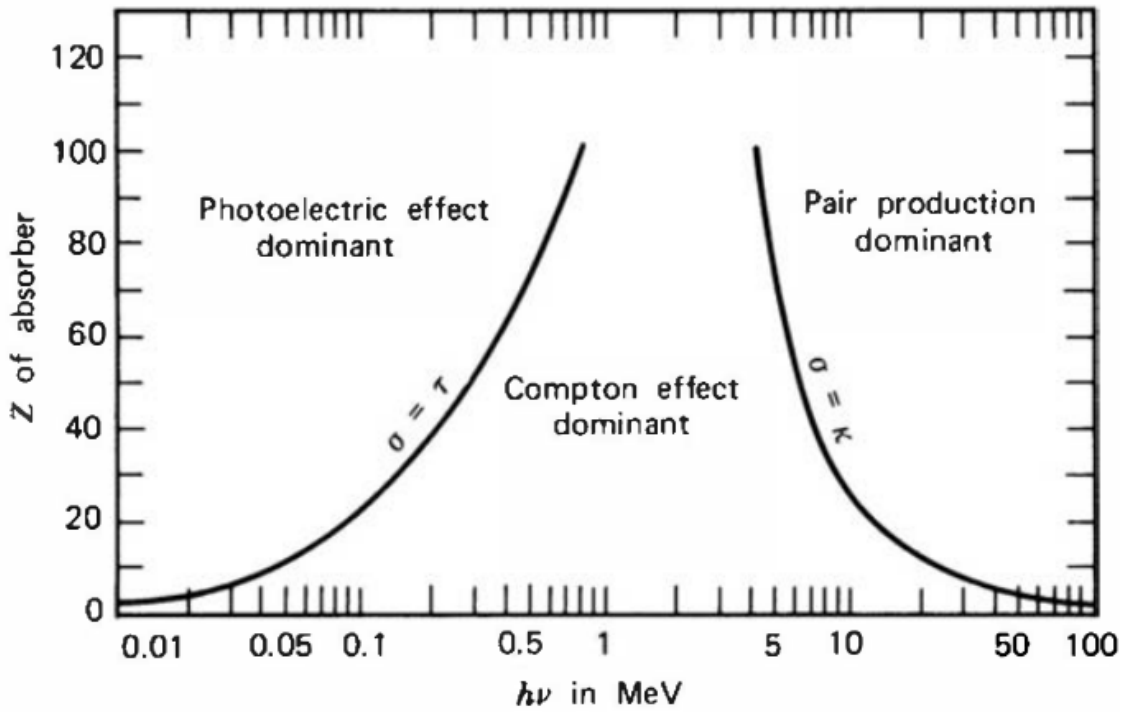


- Radiation Detection and Measurement, Glenn F. Knoll,John Wiley Sons, Inc., 2010

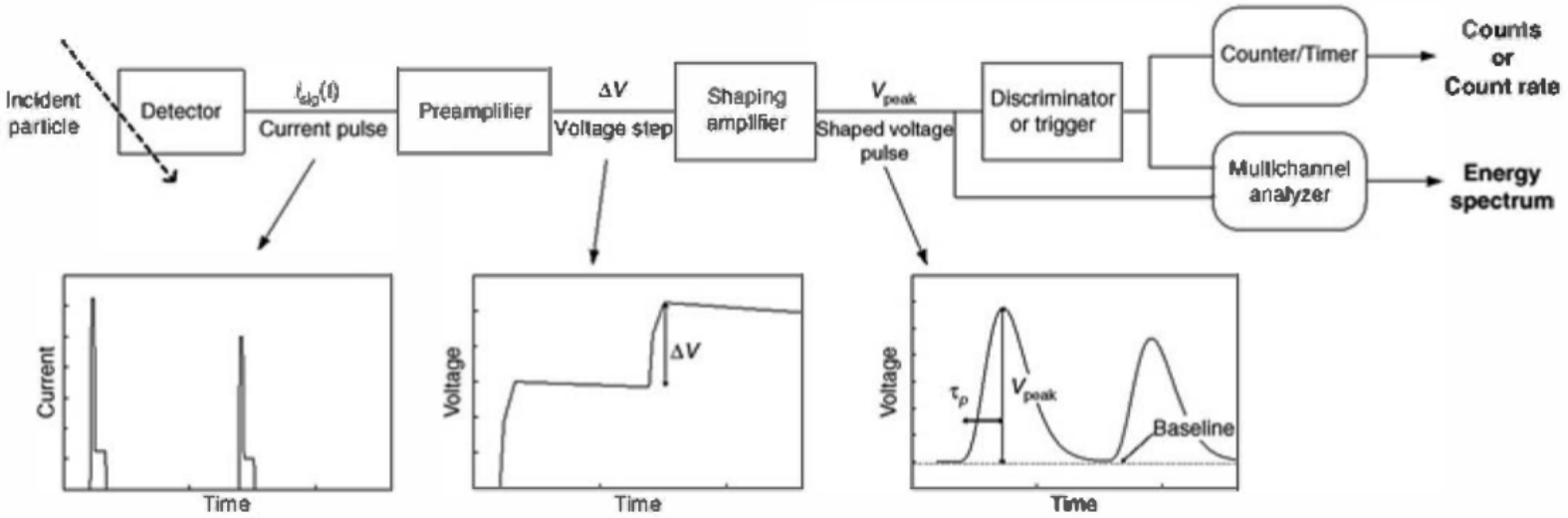


**Figure 16.1** Schematic diagram of the detector and electronics. Typical outputs from each stage of the processing electronics (for two pulses) are also sketched. (Courtesy of R. Redus, Amptek, Inc.)

- Radiation Detection and Measurement, Glenn F. Knoll,John Wiley Sons, Inc., 2010

$$-\frac{dE}{dx} = \frac{4\pi e^4 z^2}{m_0 v^2} NB$$

where

$$B \equiv Z\left[\ln\frac{2m_0v^2}{I} - \ln\left(1-\frac{v^2}{c^2}\right) - \frac{v^2}{c^2}\right]$$

- Radiation Detection and Measurement, Glenn F. Knoll,John Wiley Sons, Inc., 2010

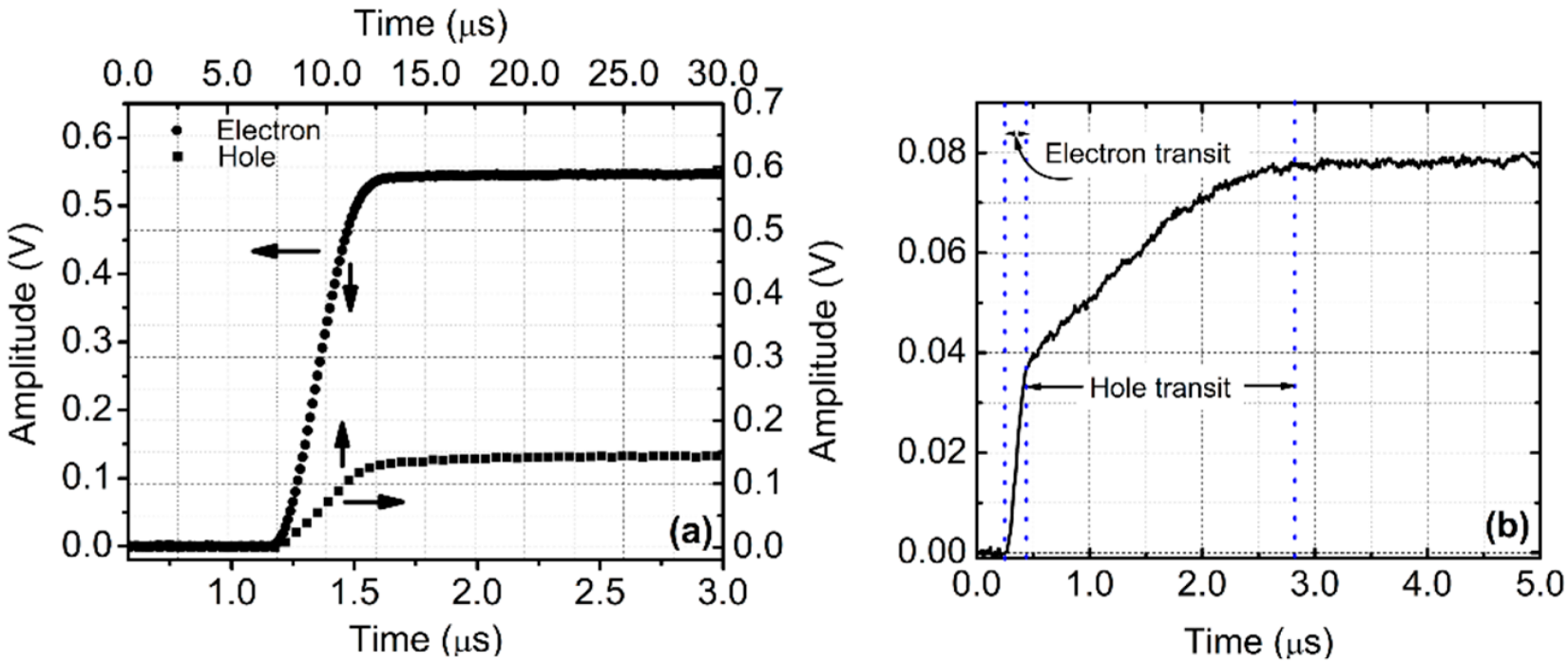


- Chaudhuri, S.K.; Kleppinger, J.W.; Karadavut, O.; Nag, R.; Mandal, K.C. Quaternary Semiconductor $Cd_xZn_xTe_ySe_y$ for High-Resolution, Room-Temperature Gamma-Ray Detection. Crystals 2021, 11, 827

# Collimator Opening Angle

- Collimator 4.26° FWHM Opening Angle

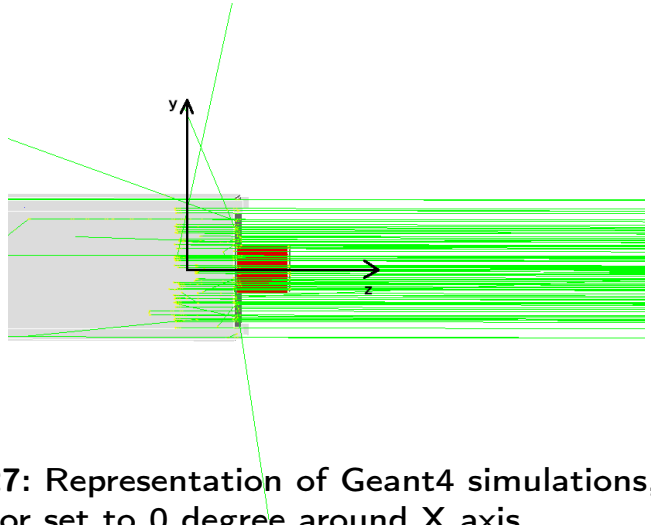


**Figure 27:** Representation of Geant4 simulations, collimator set to 0 degree around X axis.

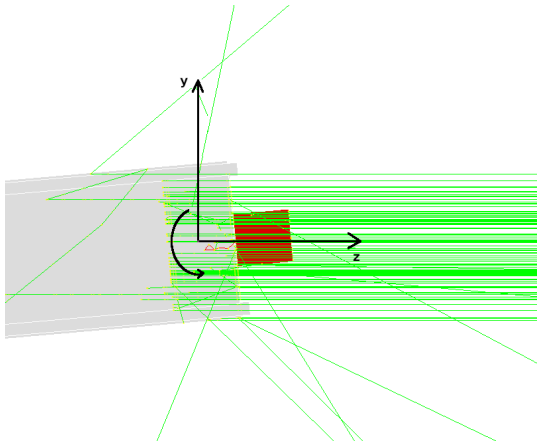


**Figure 28:** Representation of Geant4 simulations, collimator set to 5 degree around X axis.

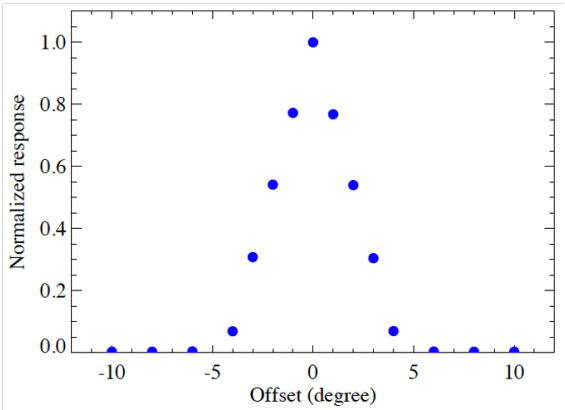


**Figure 29:** Angular response of the collimator obtained using GEANT simulations.

# Effective Area

- The maximum effective area is 5.3 $cm^2$ at 60 keV

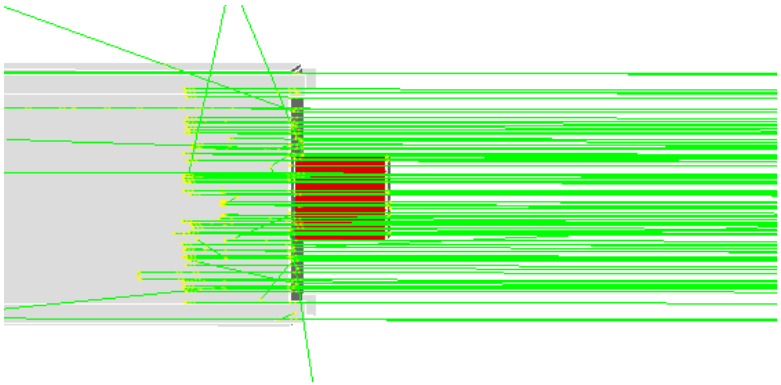

**Figure 30:** Representation of Geant4 simulations for effective area determination.

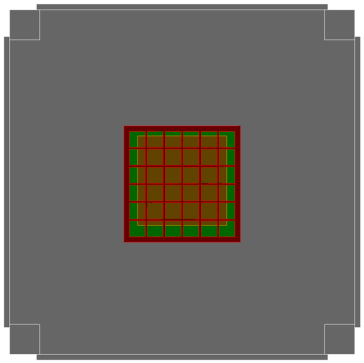

**Figure 31:** CdZnTe position inside the collimator.

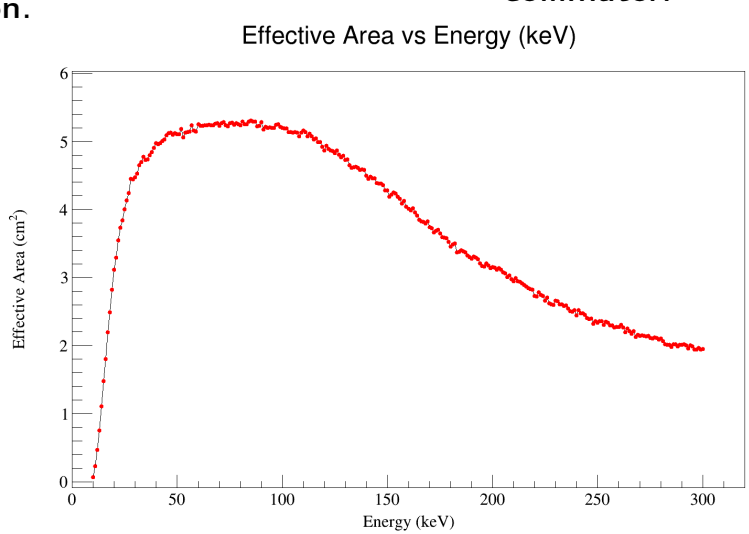


**Figure 32:** The effective area of the detector after the collimator.

# Normalization

- Flux defined as $\frac{f(E)}{dE}$, particles/cm$^2$/s/sr/keV
- Particle rate (P - particles per second), j from 1 to number of bins:

$$\mathrm{P}_j = \int dA \int d\Omega \int \frac{f(E)}{dE} dE_j \qquad (particles \quad s^{-1})$$

- How much time required to get $N_p$ of particles per bin ($N_p = 10^5$ for Albedo photons) :

$$T_j = \frac{N_p}{P_j}$$

- The total detected count rate, $C$, by the summation of the ratio of the number of the deposited particles per energy bin, $M_j$, to the observation time $T_j$.

$$C = \sum_{j=1}^{N} \frac{M_j}{T_j}$$

# Back-Shield Design

**Table 3:** The count rates for the albedo $\gamma$-rays for different back-shield design. The thickness of the back-shield is 2 mm. For the graded-Z shielding designs, the thicknesses are 0.5 mm, 1.0 mm, and 0.5 mm respectively.

| **Energy Range** | **W** (cnt/s) | **Sn-W-Cd** (cnt/s) | **Pb** (cnt/s) | **Sn-W-Cu** (cnt/s) | **Pb-Sn-Cu** (cnt/s) | **No Back-Shield** (cnt/s) |
|---|---|---|---|---|---|---|
| 20 - 60 keV | 0.12 | 0.13 | 0.12 | 0.14 | 0.16 | 0.76 |
| 20 - 200 keV | 0.37 | 0.42 | 0.43 | 0.45 | 0.51 | 2.66 |

# Total background spectrum and count rates

**Table 4:** The background count rates for the corresponding background components in the orbit. The count rates are calculated by using the deposited energies of the background particles in Geant4 simulations.

| **Energy Range** | **CDGR** (0.01-100 MeV) (cnt/s) | **Albedo** $\gamma$ (0.01-100 MeV) (cnt/s) | **GCRs** $p^+$ (0.001-100 GeV) (cnt/s) | **GCRs** $\alpha$ (0.001-100 GeV) (cnt/s) |
|---|---|---|---|---|
| $\geq$20 keV | 0.39 | 1.58 | 2.70 | 0.30 |
| 20 - 60 keV | 0.17 | 0.12 | 0.04 | 0.005 |
| 20 - 200 keV | 0.27 | 0.37 | 0.13 | 0.01 |

| **Energy Range** | **Trapped** $p^+$ (0.1-400 MeV) (cnt/s) | **Trapped** $e^-$ (0.04-7 MeV) (cnt/s) | **Albedo** $n^0$ (10 keV - 1 GeV) (cnt/s) | **Crab** (10 keV - 1 MeV) (cnt/s) |
|---|---|---|---|---|
| $\geq$20 keV | 1.01 | 0.01 | 0.02 | 1.10 |
| 20 - 60 keV | 0.01 | 0.002 | 0.005 | 0.81 |
| 20 - 200 keV | 0.02 | 0.005 | 0.01 | 1.08 |

# THEBES simulation

- Charge carriers moving along z in each grid step by step
- $v = \mu E_z = \Delta z / \Delta t$
- $\Delta t = \Delta z / (\mu E_z)$
- $\Delta x, y = \mu E_{x,y} \Delta t$
- $Q_{ind} = -Q_R(z) W(z)$, where W(z)is the weighting potential
- $Q_R(z) = Q(z-1) exp(-T/\tau)$ [9],Remaining charge
- $Q_T(z) = Q(z-1) - Q_R(z)$, Trapped charge

# THEBES simulation

- Equation determining the size of the charge distribution over time due to the diffusion and electrostatic repulsion is given by [10]

$$\frac{d\sigma(t)^2}{dt} = 2D + \frac{\mu_e N e}{12\pi^{(3/2)}\epsilon_0\epsilon_r\sigma(t)} \quad (1)$$

  - D, the diffusion constant, $D = \frac{\mu_e k_B T}{e}$
  - Number of electron-hole pairs, $N = \frac{E_\gamma}{\varepsilon}$, where $\varepsilon$ (4.6 eV) the pair creation energy.
  - $\mu_e$, the electron mobility
  - $k_B$, the Boltzmann constant
  - T, the temperature in Kelvin
- Eq. 1 solved numerically by using the Runge–Kutta method.

# iXRD Sensitivity Estimations

- Performed THEBES simulation using the calibration setup and $^{57}Co$ source.
- THEBES simulation parameters that provided the best simulated $^{57}Co$ spectra compared to the measured ones in the calibration.

**Table 5. The Simulation parameters to obtain the iXRD background Spectrum**

| THEBES Parameters | Values |
|---|---|
| Electron mobility ($mm^2/V\ s$) | $1.0 \times 10^5$ |
| Hole mobility ($mm^2/V\ s$) | $1.05 \times 10^4$ |
| Electron trapping time (s) | $3.0 \times 10^{-6}$ |
| Hole trapping time (s) | $1.0 \times 10^{-6}$ |
| Electronic noise level for anode channels | 4-7% |
| Electronic noise level for planar cathode | 6% |
| Minimum detectable energy for anodes | 20 keV |
| Minimum detectable energy for cathode | 40 keV |

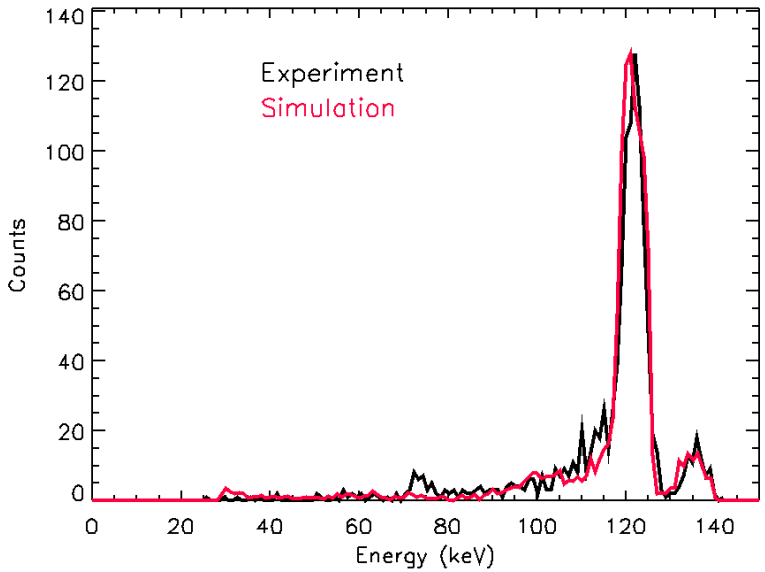


**Figure 33:** The comparison of the energy spectra for the simulations and experiments for a single channel.